nature cell biology

Adaptive changes in the kinetochore architecture facilitate proper spindle assembly

Valentin Magidson[1,5,6], Raja Paul[2,3,5], Nachen Yang[1], Jeffrey G. Ault[1], Christopher B. O'Connell[1,6], Irina Tikhonenko[1], Bruce F. McEwen[1], Alex Mogilner[3,7] and Alexey Khodjakov[1,4,7]

Mitotic spindle formation relies on the stochastic capture of microtubules at kinetochores. Kinetochore architecture affects the efficiency and fidelity of this process with large kinetochores expected to accelerate assembly at the expense of accuracy, and smaller kinetochores to suppress errors at the expense of efficiency. We demonstrate that on mitotic entry, kinetochores in cultured human cells form large crescents that subsequently compact into discrete structures on opposite sides of the centromere. This compaction occurs only after the formation of end-on microtubule attachments. Live-cell microscopy reveals that centromere rotation mediated by lateral kinetochore–microtubule interactions precedes the formation of end-on attachments and kinetochore compaction. Computational analyses of kinetochore expansion–compaction in the context of lateral interactions correctly predict experimentally observed spindle assembly times with reasonable error rates. The computational model suggests that larger kinetochores reduce both errors and assembly times, which can explain the robustness of spindle assembly and the functional significance of enlarged kinetochores.

Chromosome segregation during cell division is enacted by the mitotic 'spindle'. Chromosomes connect to the spindle through kinetochores that capture microtubules and attach to their plus ends, the principle described as 'search-and-capture' (S&C; refs 1–5). A ramification of the S&C mechanism is that kinetochore size and shape play a fundamental role in determining the efficiency and fidelity of chromosome segregation. Intuitively, larger kinetochores are expected to increase the probability of encounters between kinetochores and microtubules, which would also promote errors such as attachment of sister kinetochores to the same spindle pole (syntelic) or attachment of a single kinetochore to both poles (merotelic). Cellular regulations that minimize erroneous attachments while expediting spindle assembly remain unknown.

Here we demonstrate that the shape of the kinetochore's outer layer changes markedly and rapidly during the normal course of mitosis. At the onset of spindle assembly, sister kinetochores expand to almost completely encircle the centromere. After the formation of end-on attachments to microtubules the enlarged kinetochores downsize into small discs on opposite sides of the centromere. Computational analyses suggest that the observed reorganization of the kinetochore architecture simultaneously enhances the efficiency of microtubule capture and suppresses the number of erroneous attachments. Error reduction is due to improvements in the angular orientation of enlarged kinetochores that result from lateral interactions with microtubules before the formation of end-on attachments. If these lateral interactions are impeded, the number of errors increases significantly.

RESULTS

The outer layer of unattached kinetochores encircles the centromere

Properly attached kinetochores appear as nearly diffraction-limited spots in fluorescence light microscopy[6] (LM) and as ~200-nm discs positioned on opposite sides of the centromere in electron microscopy[7,8] (EM). However, the kinetochore outer layer is enlarged when cells are arrested in mitosis owing to a lack of microtubules[9–11]. Enlarged kinetochores have been observed also during prometaphase in HeLa cells[12]. To test the idea that kinetochore size and shape change during normal spindle assembly we detailed the kinetochore architecture at various mitotic stages.

In non-transformed human cells RPE1, the outer-kinetochore protein CenpF forms compact spots during late prophase and metaphase, but partially encircles the centromere shortly after nuclear

[1]Wadsworth Center, New York State Department of Health, Albany, New York 12201, USA. [2]Indian Association for the Cultivation of Science, Jadavpur, Kolkata 700032, India. [3]Courant Institute and Department of Biology, New York University, New York, New York 10012, USA. [4]Rensselaer Polytechnic Institute, Troy, New York 12180, USA. [5]These authors contributed equally to this work. [6]Present addresses: National Cancer Institute, Frederick, Maryland 21702, USA (V.M.); Nikon Instruments, Melville, New York 11747, USA (C.B.O'C.).
[7]Correspondence should be addressed to A.M. or A.K. (e-mail: mogilner@cims.nyu.edu or alexey.khodjakov@health.ny.gov)

Received 26 November 2014; accepted 13 July 2015; published online 10 August 2015; DOI: 10.1038/ncb3223

envelope breakdown (NEB, 193 of 274 kinetochores in 3 cells) and during prometaphase (267 of 550 kinetochores in 6 cells; Fig. 1). Despite the apparent change in morphology, the amount of CenpF at the kinetochore remains constant from prophase through prometaphase (Fig. 1c). To detail changes within the outer layer we co-visualized CenpF (ref. 13) and CenpE (refs 14,15), the two most peripheral kinetochore proteins capable of direct interactions with microtubules. CenpE appears at the kinetochores only after NEB (Fig. 2). We have previously demonstrated that the central region of forming spindles becomes devoid of chromosomes ∼1 min after NEB in RPE1 cells[16] (see Supplementary Videos 2 and 3). This feature allows one to identify cells that are in the first minute of spindle assembly. In these cells, CenpE is detected only at some of the kinetochores. Intriguingly, CenpF forms compact spots in CenpE-negative kinetochores but partially encircles the centromere in CenpE-positive kinetochores (Fig. 1d,e). As the amount of CenpF remains constant during prophase–prometaphase (Fig. 1c), relative volumes occupied by this protein can be compared. Volumetric analysis (Fig. 1f) suggests that the outer layer expands during spindle assembly.

Unlike CenpF, proteins that reside deeper inside the kinetochore (Hec1, Mis12; ref. 6) appear as compact spots throughout mitosis (Fig. 2) even though the amount of Hec1 increases during prometaphase (Fig. 2c) whereas the amount of Mis12 remains constant (Fig. 2c). The volume occupied by Mis12 also remains constant (Fig. 2g). Thus, changes in the kinetochore architecture occur primarily in the outer layers of the organelle.

To evaluate the shape of the outer layer at a higher resolution, we employed correlative LM/EM. Serial-section analyses of three cells at NEB reveal highly variable kinetochore morphology. Although the exact location of kinetochores is determined by means of correlation of LM and EM images (Fig. 3a), most of the kinetochores lack distinct plates. In one cell all kinetochores appear as ill-defined spots of fibrous material (Fig. 3b). In the other two cells, ∼30% of kinetochores (53/185) exhibit trilaminar plates that largely encircle the centromere. The gap between the plates of sister kinetochores is typically 100–200 nm on one side and larger on the other side of the centromere (Fig. 3d). The rest of the kinetochores appear as ill-defined spots or partially assembled plates embedded in a small cloud of fibrous material (Fig. 3c). These observations suggest that at the onset of spindle assembly, the outer plate rapidly expands from a compact cloud to a large crescent on the surface of the centromere.

Microtubules in the proximity of partially assembled plates indicate that microtubule-mediated forces may play a role in shaping the kinetochore outer layer[17] (Fig. 3c). To characterize the architecture of 'virgin' kinetochores that have not interacted with microtubules, we treated cells in late prophase with nocodazole and fixed them immediately after detection of NEB (Supplementary Fig. 1). As nocodazole completely depolymerizes microtubules within 2 min (ref. 17), this experimental approach produces kinetochores whose architecture is unaffected by interactions with microtubules or prolonged mitotic arrest.

CenpF immunofluorescence suggests that the outer layers of virgin kinetochores consistently form crescents that encircle the centromere (367/500 kinetochores in 10 cells). In most cases, sister kinetochores seem to fuse together on one side of the centromere with a gap on the other side of the centromere, where sister kinetochores are separated by chromatin (Supplementary Fig. 1d). Serial-section EM confirms that the outer layers of sister kinetochores partially encircle the centromere (>80 kinetochores in the three cells). Three-dimensional (3D) reconstructions of six typical centromeres suggest that the outer layers of virgin sister kinetochores cover >50% of the centromere circumference but remain separated by ∼100–200 nm (Fig. 3f).

The outer layer compacts after formation of end-on microtubule attachment

The observation that the kinetochore outer layers transition from encircling a large part of the centromere after NEB to ∼200-nm discs on the opposite sides of the centromere at metaphase[1,2] prompted us to search for the event that triggers kinetochore compaction.

Visual inspection of fluorescently labelled prometaphase kinetochores and microtubules suggests that most compact kinetochores are attached to the ends of microtubule bundles. In contrast, enlarged kinetochores either lack microtubule attachments or interact with microtubules laterally (Supplementary Fig. 2). As unambiguous discrimination of end-on versus lateral interactions is difficult in LM, we treated RPE1 cells with the CenpE (kinesin-7) inhibitor GSK-923295 (ref. 18). CenpE drives congression of chromosomes from the vicinity of the pole to the spindle equator[15,19,20] and mediates conversion from lateral to end-on attachments[21]. Partial inhibition of CenpE with 15-nM GSK-923295 results in the accumulation of mono-oriented chromosomes and prolongation of mitosis to >1 h in >80% of cells. Immunofluorescence demonstrates that outer (CenpF), core (Hec1, Mis12), and inner (CenpA–GFP) kinetochore proteins appear as compact spots on congressed chromosomes in GSK-923295-treated cells. In contrast, both CenpF and Hec1 form crescents on chromosomes that reside near the spindle poles (Fig. 4a,b).

In GSK-923295-treated RPE cells with one allele of Mad2 replaced with Mad2–Venus[22], at least one kinetochore on each mono-oriented chromosome remains Mad2-positive. Correlative LM/EM analysis of 31 Mad2-positive kinetochores in 4 cells demonstrates that these kinetochores lack end-on microtubule attachments but interact laterally with the walls of adjacent microtubules. The outer layer of these kinetochores is enlarged to 400–500 nm and is either spread alongside an adjacent microtubule bundle (Fig. 4d) or partially encircles the centromere (see Fig. 3d). In contrast, end-on attached kinetochores in the same cells are ∼200-nm discs (Fig. 4d′). This difference in the architecture of end-on attached versus laterally interacting kinetochores suggests that kinetochore compaction occurs only after the formation of end-on microtubule attachment and independently in sister kinetochores.

Intensity measurements demonstrate that kinetochores of congressed chromosomes in GSK-923295-treated cells contain as much Hec1 as in untreated metaphase cells (compare Figs 4c and 1f) whereas the amount of CenpF decreases to ∼50% of the normal metaphase level (compare Figs 4c and 1c, $P < 0.001$). In contrast, the amount of both CenpF and Hec1 on polar chromosomes is higher than seen during any stage of normal mitosis (compare Figs 4c and 1c,f, all $P < 0.001$ in each comparison). This difference suggests that kinetochores enlarge if end-on attachment is delayed. Similar increases in fluorescence intensity and morphological enlargement of the outer layer are observed when cells are arrested in the absence of microtubules (Supplementary Fig. 3).

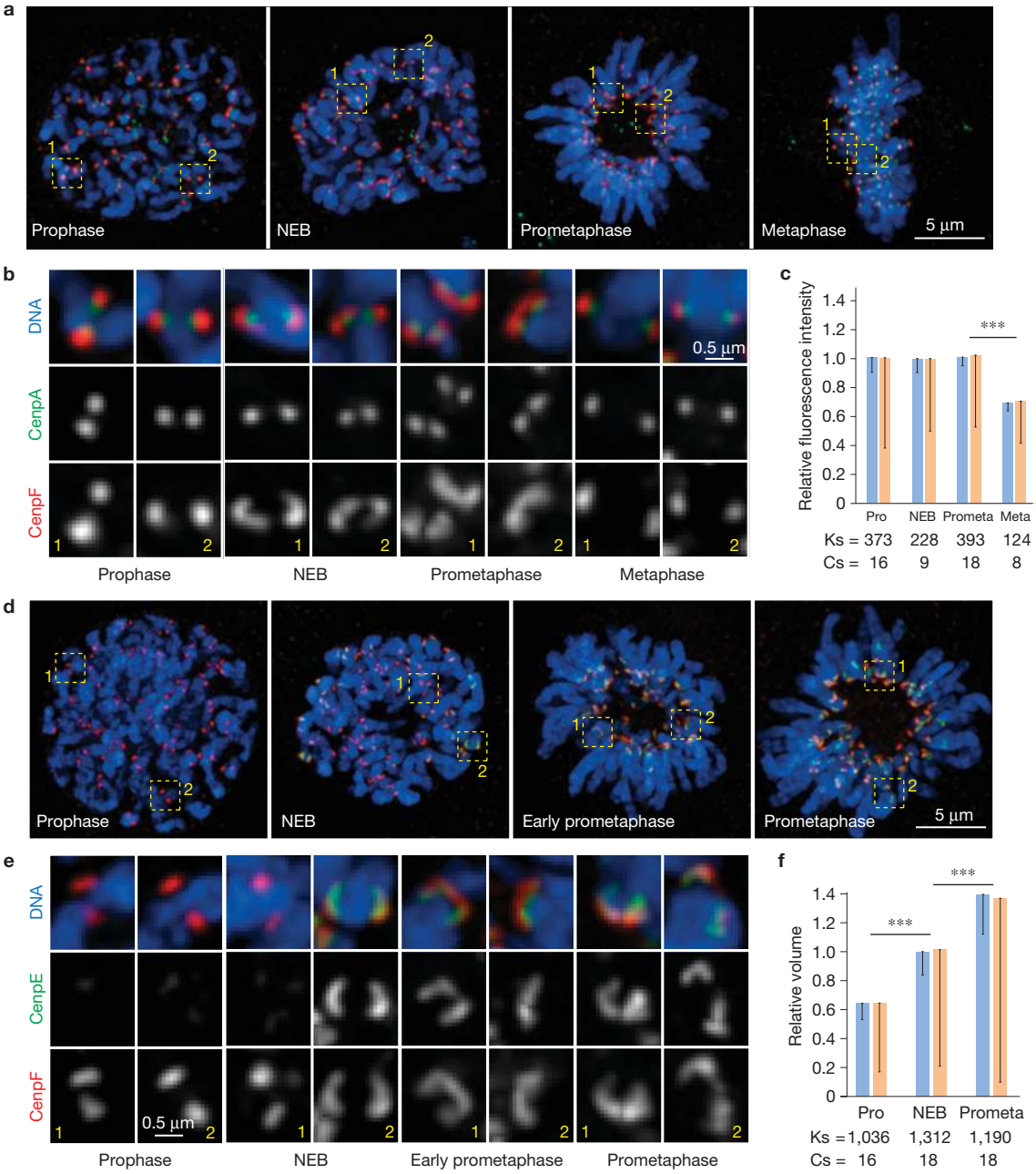

Figure 1 Changes in the outer kinetochore architecture at various stages of mitosis. (**a**–**c**) The outer layer enlarges at the onset of spindle assembly and subsequently downsizes. (**a**) Maximal-intensity projections (including all kinetochores) depicting RPE1 cells at various stages of mitosis. (**b**) Examples of individual kinetochores from the outlined areas in **a**, shown at higher magnification. The outer layers (red, CenpF) appear as compact spots during prophase and metaphase but expand into crescents that partially encircle the centromere during NEB and prometaphase. (**c**) Intensity of CenpF fluorescence remains constant during outer layer expansion and decreases during metaphase. (**d**–**f**) The outer layer both recruits additional proteins (CenpE, green) and expands (CenpF, red). (**d**) Maximal-intensity projections (including all kinetochores) depicting RPE1 cells. (**e**) Examples of individual kinetochores from the outlined areas in **d**, shown at higher magnification. (**f**) The volume occupied by CenpF increases from late prophase to prometaphase. Blue bars in **c** and **f** are calculated as the mean of the mean values for multiple kinetochores in individual cells (*n* values listed below the bars, Cs; cells). Error bars represent standard error of the mean (s.e.m.). Yellow bars are mean values calculated for all kinetochores, pooled from all cells in that class (*n* values listed below the bars, Ks; kinetochores). Error bars represent standard deviation (s.d.). Triple asterisks denote differences with $P < 0.005$ (two-tailed Student's *t*-test) for both blue versus blue and yellow versus yellow bars.

Large compactable kinetochores support rapid and low-error microtubule capture

Our observations that the outer layers of sister kinetochores rapidly expand to encircle the centromere at the onset of spindle assembly and subsequently compact into small discs on formation of end-on microtubule attachments are consistent with previous reports in various types of mammalian[9,12,23] and fly cells[24,25]. However, in the context of the S&C mechanism, kinetochore enlargement at the onset of mitosis

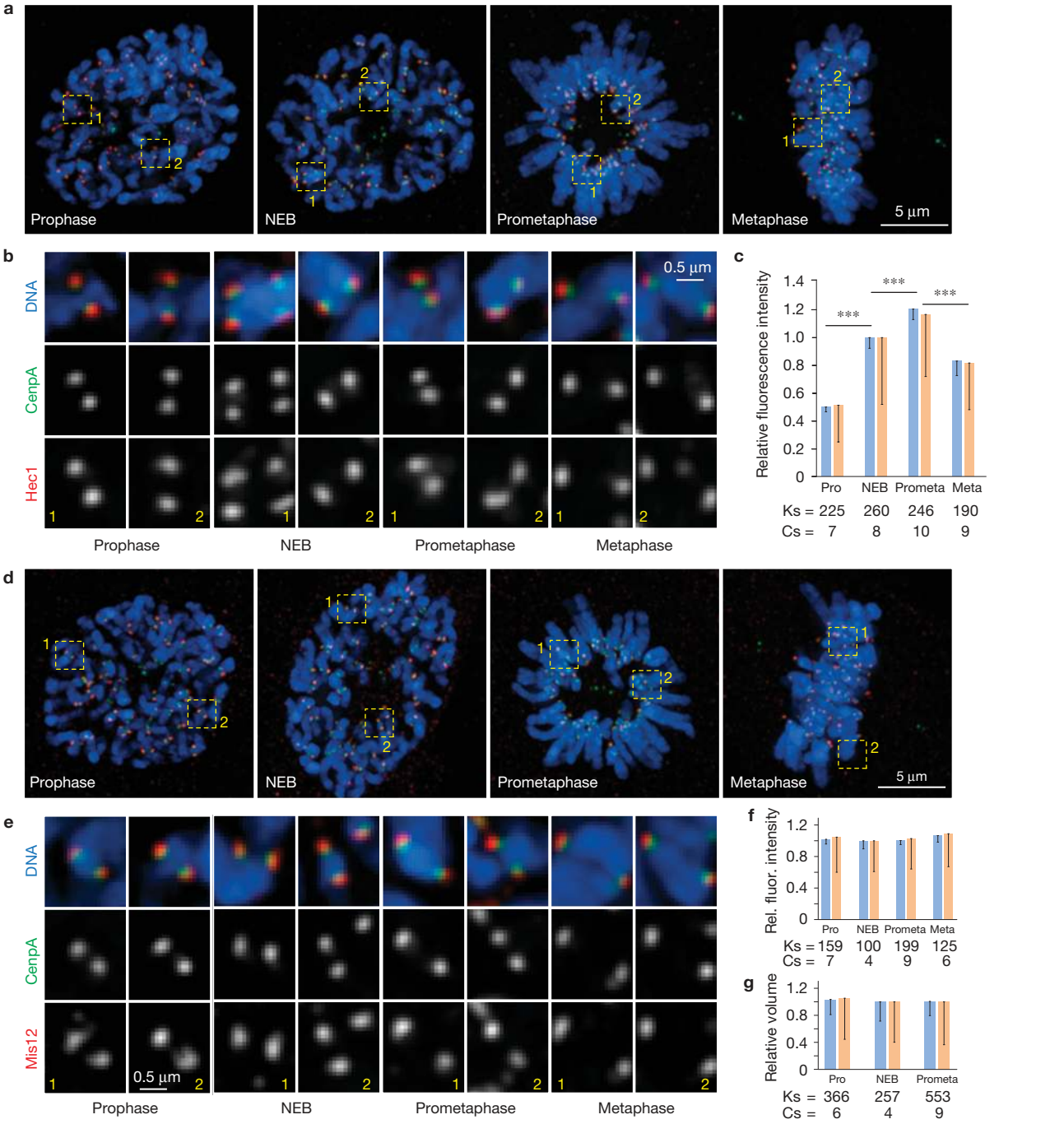

Figure 2 The kinetochore core remains relatively compact throughout mitosis. (**a**–**c**) The distribution of the core kinetochore component Hec1 is similar throughout mitosis (**a**,**b**, red) in spite of a significant increase in the amount of this protein during NEB and prometaphase (**c**). (**d**–**f**) The distribution of Mis12 (**d**,**e**, red), the amount (**f**) and the volume occupied by this protein (**g**) remain constant throughout mitosis. Also note that the shape of the inner kinetochore remains compact throughout mitosis (green, CenpA–GFP). (**a**,**d**) Maximal-intensity projections (including all kinetochores) depicting RPE1 cells at various stages of mitosis. (**b**,**e**) Examples of individual kinetochores from the outlined areas in **a** and **d** shown at higher magnification. Blue bars in **c**,**f** and **g** are calculated as the mean of the mean values for multiple kinetochores in individual cells (*n* values listed below the bars; Cs, cells). Error bars represent s.e.m. Yellow bars are mean values calculated for all kinetochores pooled from all cells in that class (*n* values listed below the bars; Ks, kinetochores). Triple asterisks denote differences with $P < 0.005$ (two-tailed Student's *t*-test) for both blue versus blue and yellow versus yellow bars.

seems counterproductive because large kinetochores are expected to increase attachment errors. Indeed, kinetochore enlargement during mitotic arrest is postulated to drive the pronounced increase in attachment errors in nocodazole washout experiments[26].

To explore potential effects of kinetochore enlargement on the number of erroneous attachments we employed computational modelling. In minimalistic stochastic models of spindle assembly, randomly located chromosomes are expected to form stable

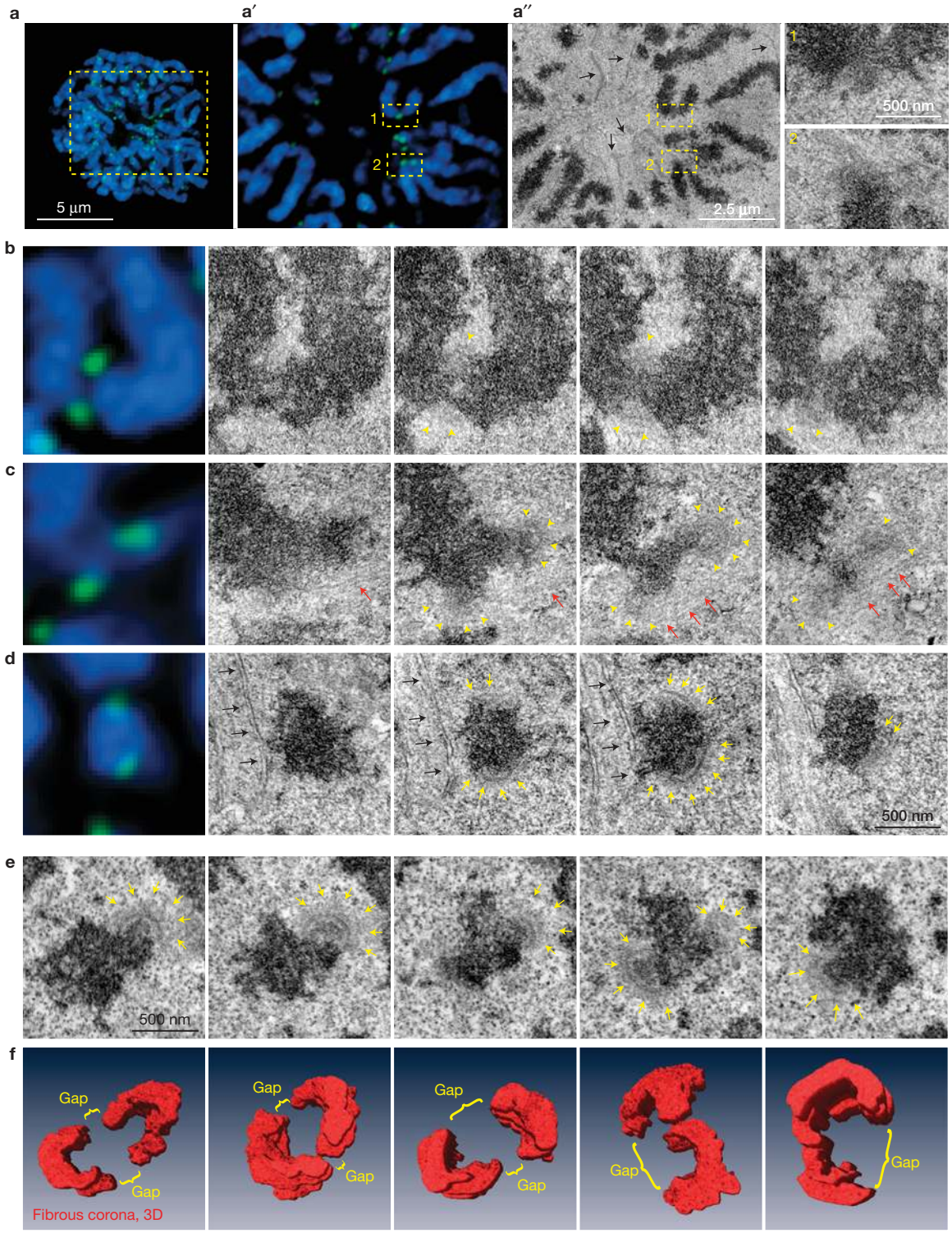

Figure 3 Kinetochore morphology at the onset of spindle assembly. (**a**) Correlative LM/EM analysis of kinetochore morphology at NEB. Maximal-intensity projection of the entire cell and an individual focal plane are shown. Through correlation of LM (**a′**) and EM (**a″**) images, positions of individual kinetochores are identified. Outlined areas are shown at higher magnification. Kinetochore 1 lacks the distinct trilaminar plate. Black arrows mark partially disassembled nuclear envelope. (**b**–**d**) Examples of kinetochore morphology in RPE cells at NEB. Each chromosome is shown in LM (left) and serial EM sections. Approximately 50% of kinetochores are morphologically indistinct (**b**). The other 50% exhibit partially (**c**), or fully assembled plates that largely encircle the centromere (**d**). Arrowheads denote fibrous corona; arrows point at distinct trilaminar plates. (**e**,**f**) Morphology of 'virgin' kinetochores in a cell fixed less than 2 min after NEB in the absence of microtubules (see Supplementary Fig. 2 for whole-cell view and preparation details). (**e**) Complete series of sections through sister kinetochores. Yellow arrows mark trilaminar plates; red arrows point at microtubules; black arrows mark remnants of nuclear envelope. (**f**) Examples of 3D reconstructions of the outer layer (first image corresponds to the kinetochores shown in **e**). The outer layers largely encircle the centromere.

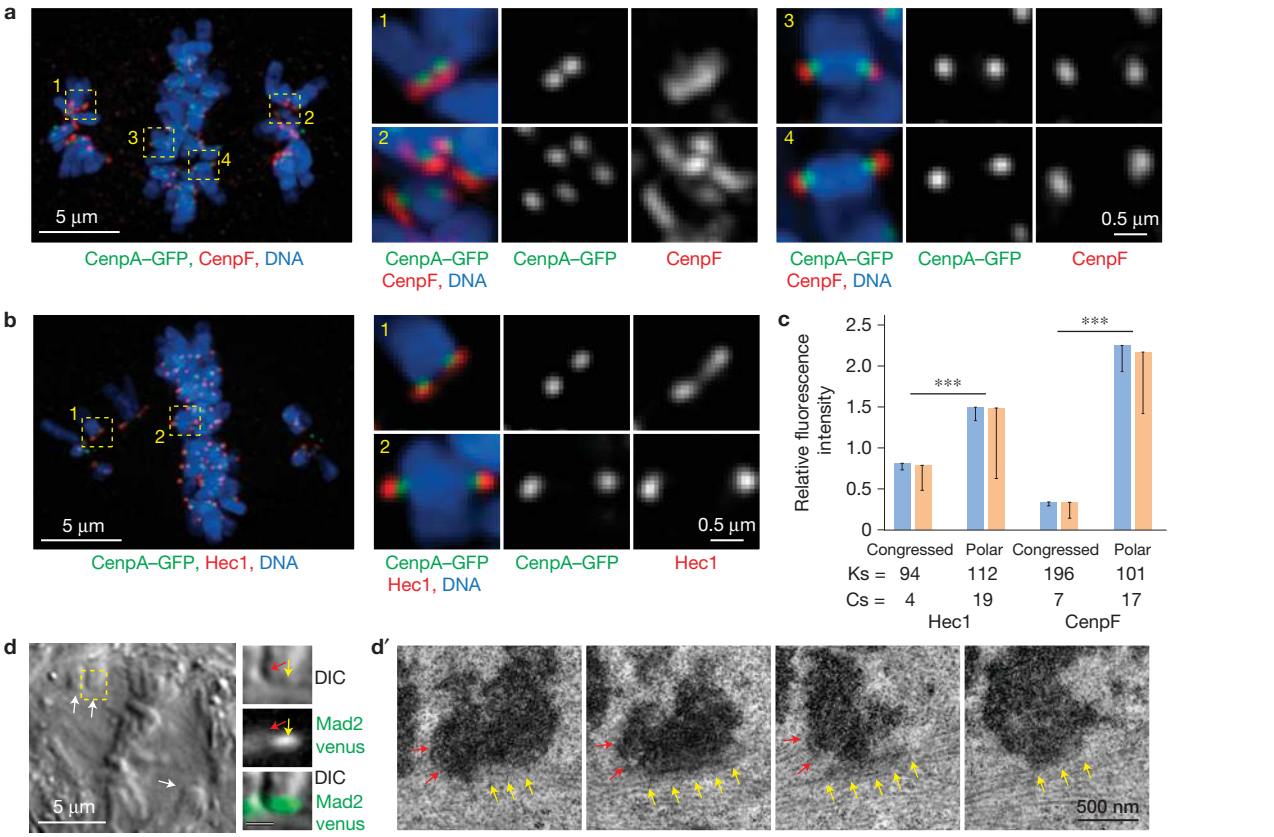

Figure 4 Kinetochore outer layer compaction occurs on the formation of end-on microtubule attachments. (**a**,**b**) Kinetochores are enlarged on polar, but compact on congressed, chromosomes. Whole-cell images are maximal-intensity projections that include all kinetochores in the cell. Individual kinetochores are shown as maximal-intensity projections. CenpF delineates the outer layer (**a**) and Hec1 delineates the kinetochore cores (**b**). (**c**) Amounts of both CenpF and Hec1 are increased on polar chromosomes. Blue bars are the mean kinetochore intensity calculated as the mean of the mean values for multiple kinetochores in individual cells (*n* values are listed below the bars. Cs: cells). Error bars represent s.e.m. Yellow bars are mean values calculated for all Ks kinetochores pooled from all cells in that class (*n* values listed below the bars. Ks; kinetochores). Error bars represent s.d. Triple asterisks denote differences with $P < 0.005$ (two-tailed Student's *t*-test) for both blue versus blue and yellow versus yellow bars. (**d**,**d′**) Sister kinetochores on congressing chromosomes exhibit distinctly different morphologies. (**d**) A single-plane differential interference contrast (DIC) image of the cell near the centre of the mitotic spindle. Arrows denote congressing chromosomes. The centromere region of one congressing chromosome (yellow outlined) is also shown at higher magnification in DIC and Mad2–Venus fluorescence (bar = 1 μm). Arrows point at the approximate positions of the leading (yellow) and trailing (red) kinetochores. (**d′**) Consecutive 80-nm electron microscopy sections through the centromere of the chromosome shown in **d**. Note the size difference between the trailing end-on attached kinetochore (red arrows) versus the leading kinetochore (yellow arrows) that lacks end-on attachment but interacts with microtubules laterally. The cells are treated with 15-nM GSK 923295, a cell-permeable inhibitor of CenpE to slow down chromosome congression and conversion from lateral to end-on microtubule attachments.

end-on microtubule attachments instantaneously when a growing microtubule plus end runs into a kinetochore. Microtubule capture by sister kinetochores is uncorrelated and the kinetochore that has already attached to a microtubule can acquire an additional connection if it is hit by another microtubule. Thus, after the initial formation of monotelic attachment, the next capture is by chance correct or erroneous (results in syntelic or merotelic attachments)[27–30].

A major limitation of these simplistic models is that they predict unrealistically long times for spindle assembly due to a low probability of encounters between microtubules and 200-nm small kinetochores[27]. Our experimental observations suggest that the size of the capture target was underestimated in these models, which prompted us to replace small discoid kinetochores with large crescents (Supplementary Fig. 4a) that become compact after microtubule attachment. The duration of compaction (τ_{comp}, Supplementary Fig. 4b) is not directly revealed in our experimental analyses. Therefore, we explored various compaction times and found that this parameter does not significantly affect the time of spindle assembly or the number of errors (Supplementary Fig. 4d,d′). Enlarged kinetochores accelerate the time of spindle assembly to 5–11 min (Supplementary Fig. 4e), which is in agreement with the observation that the metaphase plate forms in ~8 min in RPE1 cells[16]. However, the number of erroneous attachments predicted by this simulation is large (>30%, Supplementary Fig. 4e).

We have previously suggested that the number of erroneous attachments is reduced by the rotation of the chromosome that occurs immediately on the initial capture[28]. This rotation orients the centromere so that its axis (the line connecting the centres of sister kinetochores) becomes roughly parallel to the captured microtubule (Fig. 5a). As a result, the unattached sister kinetochore is less likely to capture microtubules from the same spindle pole as its sister, which suppresses attachment errors[28].

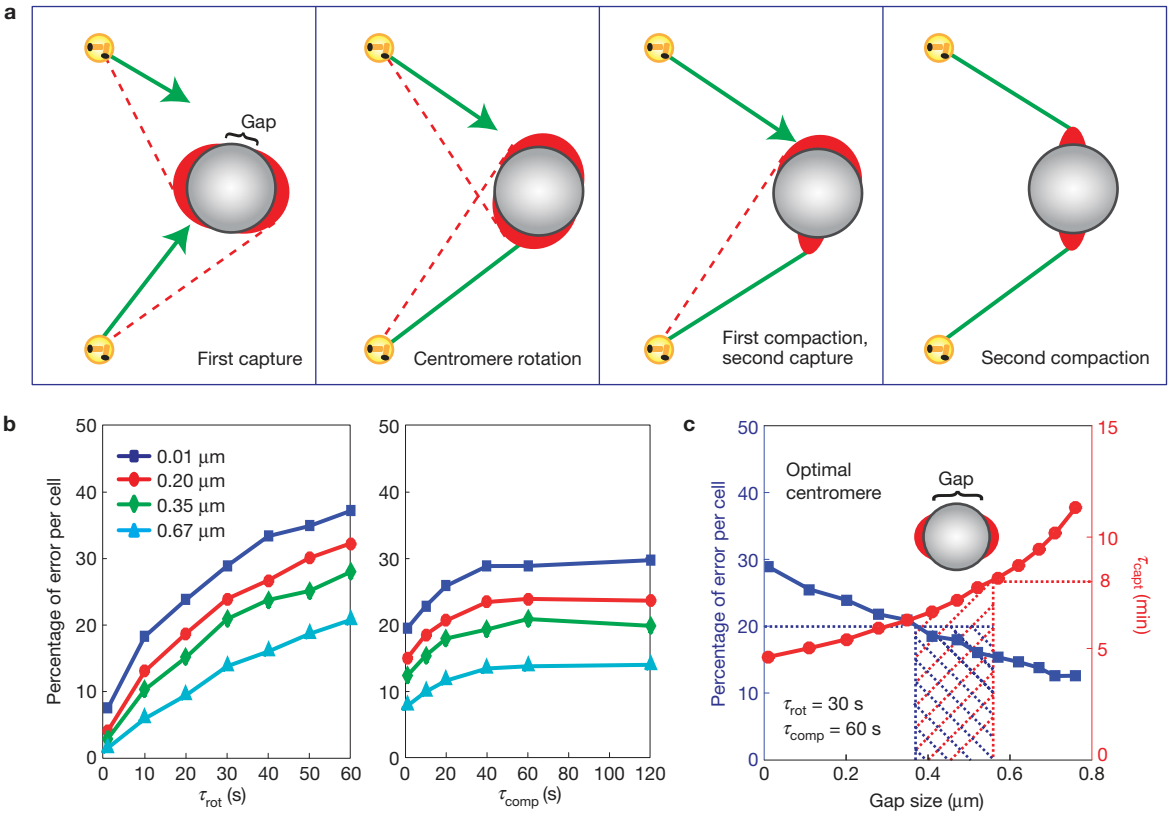

Figure 5 Effects of kinetochore enlargement–compaction on the efficiency and fidelity of capture-driven spindle assembly. (**a**) Cartoon of the events suggested in this model. Kinetochores are shown as red crescents. Green lines represent properly attached microtubules; red lines represent potential erroneous attachments. (**b**) Error frequencies predicted at various gap sizes for various rotation and compaction times. (**c**) The frequency of errors and duration of spindle assembly for different gap sizes at specific rotation and compaction times. Shaded area represents the range of parameters that result in all chromosomes attaching in <8 min with <20% of errors. The predicted optimal geometry of the centromere is shown as an inset in **c**. Note that the predicted optimal geometry is not similar to the centromere architecture observed in prometaphase cells (Fig. 3).

Simulations that consider both rotation and compaction of initially large crescent-shaped kinetochores suggest that rapid rotations significantly reduce the errors. Such rapid rotations (~30 s) have been directly observed in live cells[16]. Similarly, the errors are suppressed if kinetochores compact in <60 s (Fig. 5b). At the conservatively pessimistic parameters of $\tau_{rot} = 30$ s and $\tau_{comp} = 60$ s, the model predicts similar capture times but lower error rates (12–30%, Fig. 5c) than simulations without the rotation. However, owing to the inverse relationship between the speed of spindle assembly and the number of errors, efficient mitosis seems to require a specific and highly uniform geometry of the centromere (Fig. 5c). For example, spindle assembly in ≤8 min at the error rate ≤20% is predicted for a narrow range of gaps between sister kinetochores (0.35–0.55 µm, Fig. 5c). This prediction is ill compatible with the robustness of cell division[31] and the observed variability in the centromere architecture (Fig. 3f). Specifically, the 0.1–0.2 µm gaps observed on many virgin centromeres (Fig. 3f) would lead to >25% errors.

Lateral interactions that precede formation of end-on attachments increase robustness of spindle assembly

Difficulties in reconciling simulations with experimental observations prompted us to re-evaluate a fundamental assumption embedded in all existing computational models of spindle assembly—that the formation of microtubule attachment is a single-step process. *In vivo* observations reveal that formation of end-on attachments is preceded by lateral interactions between the kinetochores and the walls of microtubules[4,16,32,33]. These interactions dominate during early prometaphase when centromere axes become partially aligned with the spindle axis[16,33]. The extent of this angular alignment is similar in cells rendered incapable of forming end-on attachments[34] by depletions of the NDC80 component Nuf2 (ref. 16). Thus, the angular alignment is driven primarily, if not exclusively, by lateral interactions between kinetochores and microtubules.

To gain further insights into the role of lateral interactions during incorporation of a chromosome into the spindle, we used flattened RPE1 cells that express a fluorescent fusion of the checkpoint protein Mad2 (ref. 22). Correlative LM/EM demonstrates that lateral interactions do not remove Mad2 from the kinetochores (Fig. 4), which provides a readout for the formation of end-on attachment. The prolonged mitosis in flattened cells, with some chromosomes attaching to microtubules only during late prometaphase[35], enables us to follow the behaviour of individual chromosomes during their incorporation into the spindle. Time-lapse recordings of 26 chromosomes in 17 cells demonstrate that centromeres rotate to roughly align with the spindle axis while Mad2–Venus is still present on both sister kinetochores (Fig. 6). The disappearance of Mad2

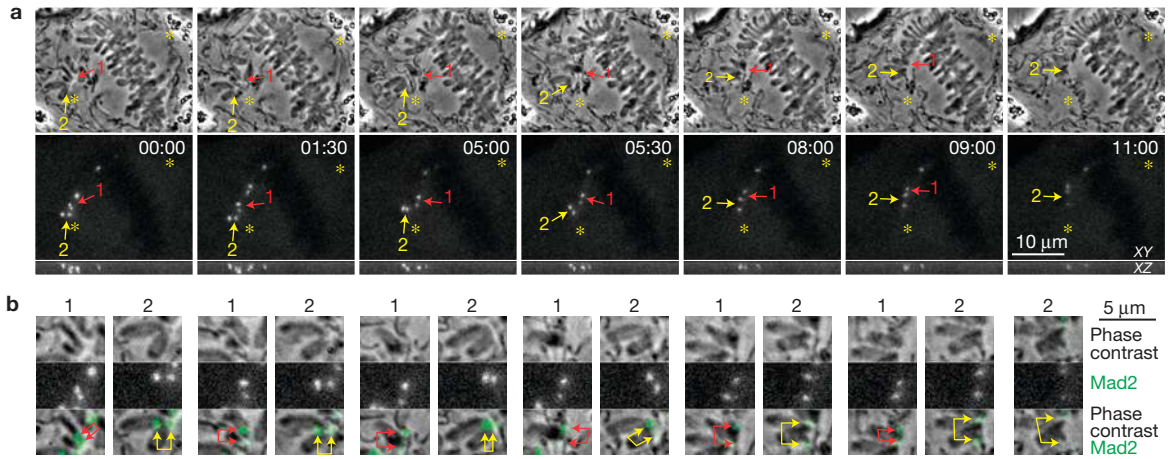

Figure 6 Centromere rotation on the surface of the spindle precedes formation of end-on microtubule attachment. (**a**) Selected frames from a multi-mode time-lapse recording of a RPE1 cell flattened to 3-μm (see Supplementary Video 1 for full recording). The top row shows phase contrast (medial slice) and the bottom row shows Mad2–Venus fluorescence (maximal-intensity projections). Both kinetochores on mono-oriented chromosomes are Mad2-positive (arrows) indicating the absence of end-on attachments. Rapid rotation that orients centromere axes roughly parallel to the spindle axis precedes chromosome congression and release of Mad2 from the kinetochores. (**b**) Higher-magnification view of the centromere marked 1 (red arrows) and 2 (yellow arrows). Note that the centromeres become stretched only during congression shortly before the release of Mad2 from the kinetochores. The cell is in a chamber that restricts mitotic rounding to ~3 μm.

from the kinetochores occurs 5–15 min after the centromere becomes roughly aligned with the spindle axis and initiates congression to the spindle equator (Fig. 6 and Supplementary Video 1). This behaviour supports the idea that centromere rotation precedes formation of end-on attachments.

On the basis of these observations, we modified the model to incorporate a two-step process in which centromere rotation, mediated by lateral kinetochore–microtubule interactions, precedes microtubule end-on capture (Fig. 7a). We postulate that the centromere rotates until the interacting microtubule reaches the edge of the kinetochore at the gap (Supplementary Fig. 5a). Lateral interactions are expected to initiate within seconds after NEB (ref. 16).

Simulations that consider centromere rotations before end-on attachment predict that larger kinetochores increase both the speed and accuracy of the spindle assembly. Unlike in all previous models, the relationship between the speed and accuracy of spindle assembly is not inverse and the <20% of error rate is predicted for a much wider range of gap sizes than in the 'attachment–rotation' scenario (compare Figs 7c and 5c). Incorporation of both types of centromere rotation (one driven by lateral interactions and one resulting from end-on attachment) into the model decreases the number of errors to ~10–15%, and the error rate becomes largely insensitive to the kinetochore size. With any gap size <0.5 μm, the assembly time is <8 min, and the error rate is <15% (Fig. 7e). Interestingly, the lowest error rate (Fig. 7e) is predicted when the gap between sister kinetochores is the commonly observed ~0.2-μm (Figs 2 and 3). Thus, lateral interactions that precede formation of end-on attachments increase robustness of spindle assembly.

Deviant geometry of the nascent spindle increases chromosome mis-segregation

Our model suggests that the kinetochore architecture is adapted for spindle assembly that involves partial angular alignment of centromeres that normally occurs on the surface of a nascent spindle before the formation of end-on attachments[16]. If pre-alignment is impeded, enlarged kinetochores would lead to an increase in the number of errors (Fig. 5c). This prompted us to evaluate the organization of the early prometaphase spindle in cells that mis-segregate chromosomes.

The largest frequency of centromere rotations is observed during early prometaphase[16] when the centromeres reside on the surface of a nascent spindle (Fig. 8a). This pattern forms in most RPE1 cells (>90% (47/50)). We find that those untreated RPE1 cells that fail to form the clear zone (3/50) are prone to exhibit lagging chromosomes during anaphase (Fig. 8b). To experimentally impede formation of the clear zone, we treated RPE1 cells with 3-μM nocodazole (for <30 min), located cells that just entered mitosis, washed out the drug, and followed formation of the spindle by 3D time-lapse microscopy. Under these conditions, the clear zone consistently fails to form ($n=21$) and the centromeres are intermixed with microtubules, which impedes angular alignment of the centromeres. Forty-three per cent of the nocodazole-treated cells (9/21) exhibit lagging chromosomes during anaphase–telophase (Fig. 8c). Therefore, a lack of a clear zone in the centre of the nascent spindle correlates with an increased frequency of errors.

DISCUSSION

Direct observations of microtubule capture by kinetochores[4,32] have established S&C (ref. 5) as the basic principle of spindle assembly. Multiple mechanisms such as the spatially selective stabilization of microtubules by RanGTP (ref. 36), the rotation of chromosomes[28], the formation of a specific spatial arrangement during early prometaphase[16], and the sweeping movements of growing microtubules[37] promote microtubule capture and thus accelerate spindle assembly. However, the inverse relationship between the efficiency and accuracy of S&C-driven spindle formation inherent

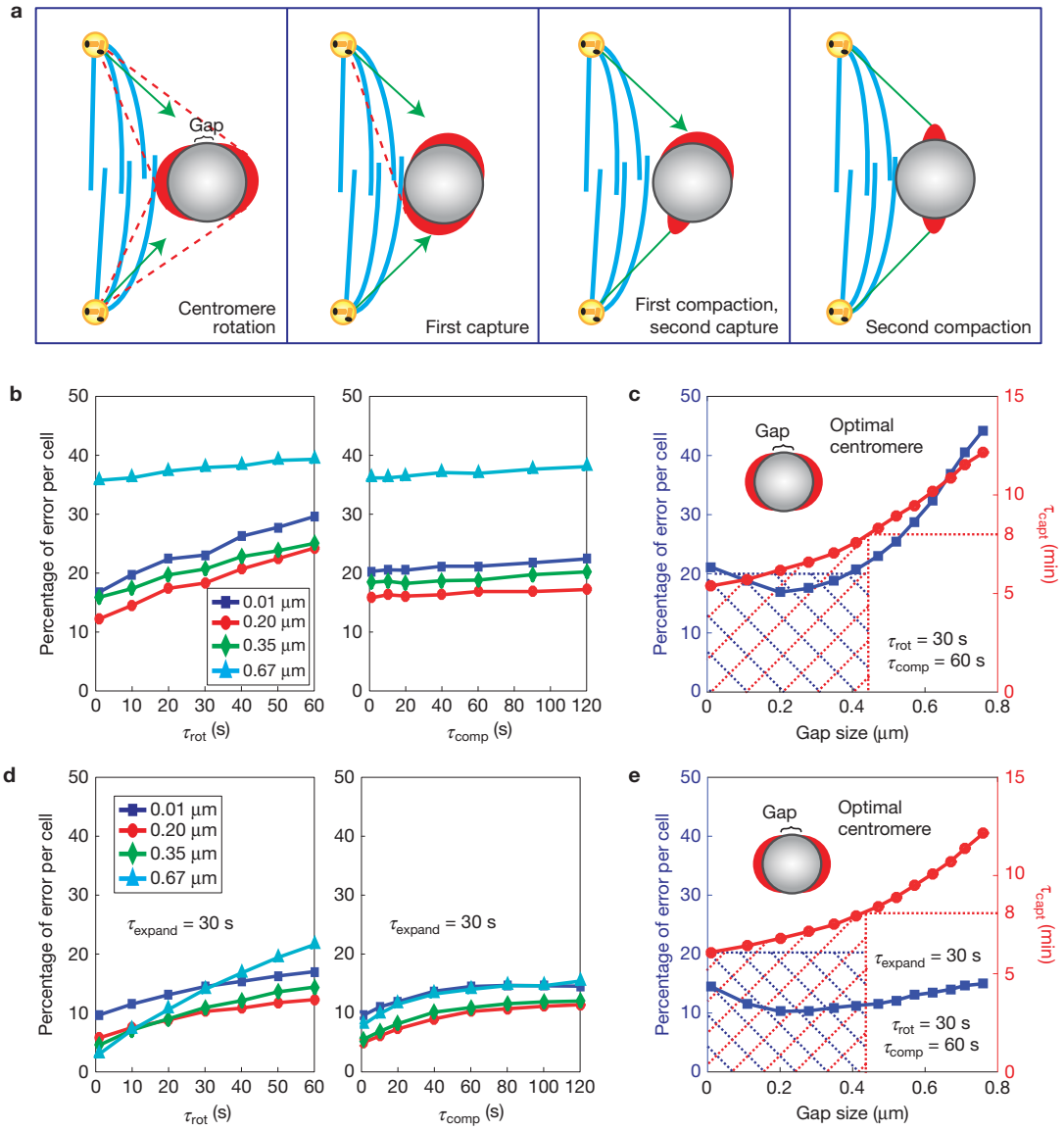

Figure 7 Computational models that consider centromere rotation due to lateral interactions with microtubules predict experimentally observed parameters of spindle assembly. (**a**) Cartoon of the events suggested in the model. Blue lines represent the central part of the nascent spindle with a high density of microtubules and devoid of chromosomes. Kinetochores can glide alongside these microtubules resulting in a rotation of the centromere. Green lines represent properly end-on attached microtubules; red lines represent potential erroneous attachments. (**b**,**c**) Results of the simulation that considers a single centromere rotation that takes place before end-on microtubule attachment and is driven by lateral interactions. (**b**) Error frequencies predicted for various gap sizes at various rotation and compaction times. (**c**) Error frequencies and durations of spindle assembly for various gap sizes at conservatively estimated rotation and compaction times. (**d**,**e**) Results of the all-inclusive simulation that considers expansion and compaction of the kinetochore as well as two subsequent rotations: one driven by lateral interactions (as in **b**,**c**) and one that results from the end-on microtubule attachment (as in Fig. 5b,c). (**d**) Error frequencies predicted for various gap sizes at 30-s expansion time and various rotation and compaction times. (**e**) Error frequencies and durations of spindle assembly for various gap sizes at specific expansion, rotation and compaction times. Shaded areas in **c** and **e** mark the range of parameters that result in all chromosomes attaching in <8 min with <20% of errors. Predicted optimal geometry of the centromere is shown as insets in **c** and **e**. Note the similarity of the predicted optimal geometry to the experimental observations (Fig. 3).

in all previous computational models is incompatible with the well-established robustness of mitotic regulations.

Our observation that the kinetochore outer layer expands at the onset of mitosis demonstrates that previous computational models underestimated the size of microtubule-capturing target. By introducing adaptable kinetochore geometry and pre-alignment of centromeres due to rapid lateral kinetochore–microtubule interactions before the formation of end-on microtubule attachments[4,16,32,33,38], we have constructed the first model that predicts realistically rapid spindle assembly with error rates that are sufficiently low to be handled by error-correction mechanisms[26,39,40]. A non-trivial prediction of our model is that kinetochore expansion during the phase of spindle assembly when lateral interactions dominate creates a synergistic relationship between the efficiency and fidelity of spindle assembly.

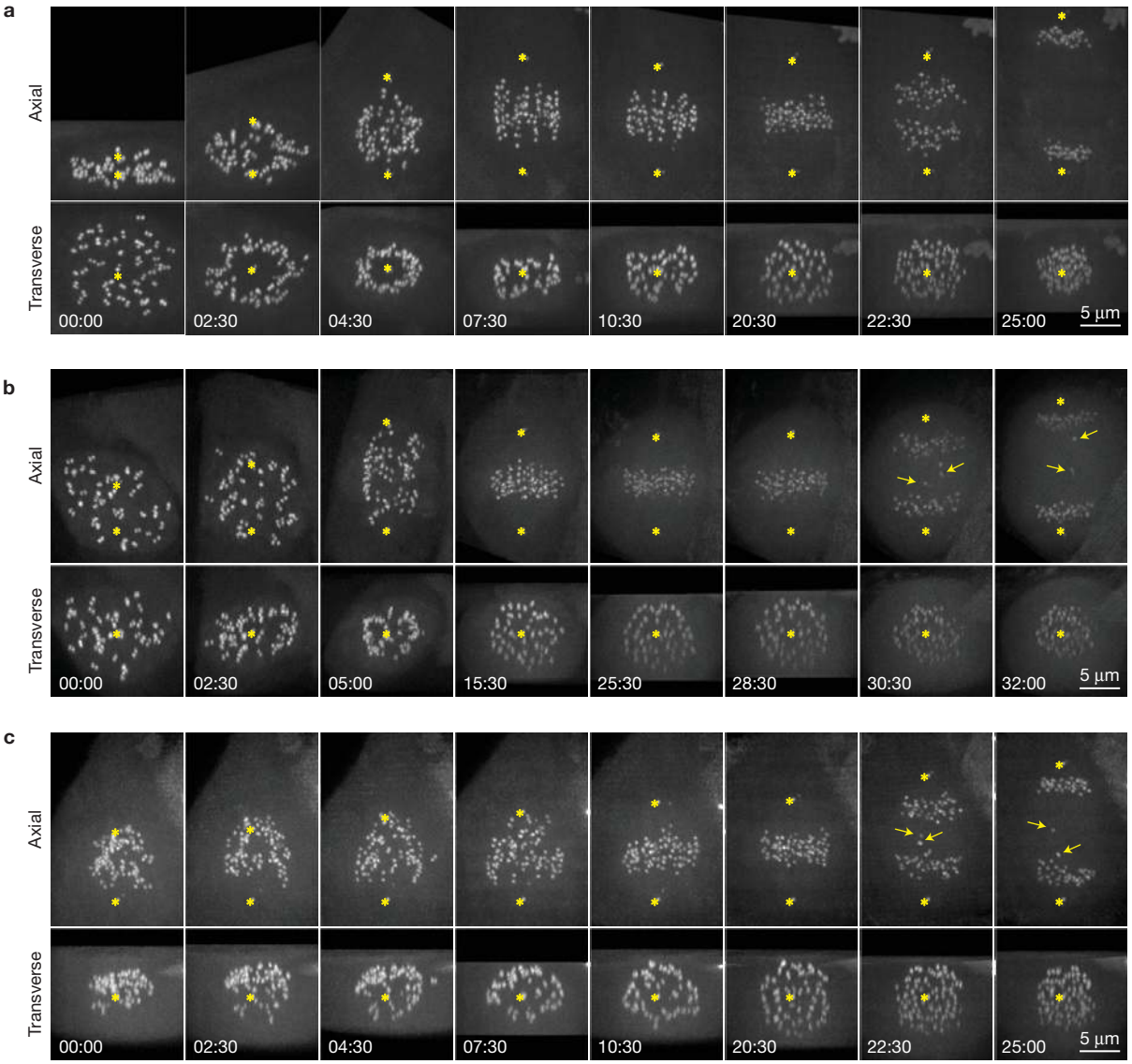

Figure 8 Abnormal geometry of the nascent spindle during early prometaphase correlates with erroneous chromosome segregation. (**a**) Typical pattern of spindle formation (RPE1 cell). Note that all centromeres (CenpA–GFP) reside on the surface of the nascent spindle for the first 6–8 min of prometaphase. (**b**) Example of an untreated RPE1 cell where the formation of the clear central zone fails for unknown reasons. The centromeres are interspersed from the onset of spindle assembly. Although all chromosomes congress onto the metaphase plate with only a minor delay, several chromosomes lag behind during anaphase (arrows), which is indicative of erroneous kinetochore attachments. (**c**) Spindle assembly after nocodazole washout. Formation of the clear central zone does not occur and chromosomes are lagging during anaphase (arrows). Asterisks mark mother centrioles (labelled with centrin–GFP). To ensure the detection of the clear zone each time point is rotated and shown as maximal-intensity projections in precisely axial and transverse orientations. See Supplementary Fig. 6 and Supplementary Videos 3–5 for conventional views of these cells. Time in minutes:seconds from NEB (**a**,**b**) or completion of nocodazole washout (**c**).

This can explain the robustness of the process in spite of the inevitable size variation of individual kinetochores in real cells. A corollary of this prediction is that conditions that impede domination of lateral interactions during the initial stages of spindle assembly increase the number of erroneous attachments.

Centromere alignment by means of lateral interactions primarily takes place when centromeres reside on the surface of the nascent spindle[16,33]. Therefore, conditions that affect the formation of the hollow spindle during early prometaphase are deleterious for chromosome segregation. Consistent with this notion, attachment errors are consistently observed in cells depleted for chromokinesins[41,42], a condition that has been shown to disrupt formation of the ring[16]. Further, chromosomes tend to mis-segregate when microtubules and centromeres become intermixed during early prometaphase owing to 'reversible' drug treatments (Fig. 8) or transient deviations from the proper geometry in cells with abnormal centrosomal activity[43–46]. Subtle and transient changes in the geometric constraints during the initial stages of spindle assembly may still have devastating consequences for genomic stability even when the architecture of the mature metaphase spindles is not directly affected. □

METHODS

Methods and any associated references are available in the online version of the paper.

Note: Supplementary Information is available in the online version of the paper

ACKNOWLEDGEMENTS

This work was supported by NIH grant GM059363 to A.K. and NSF grant DMS-1118206 to A.M. The Electron Microscopy was enabled by the use of the Wadsworth Center's Electron Microscopy Core Facility. We thank J. Pines (University of Cambridge, UK) for his generous donation of Mad2–Venus cells and S. Li (Air Worldwide, USA) for assistance with the intensity quantifications.

AUTHOR CONTRIBUTIONS

A.K. and B.F.M. designed the experiments, V.M., N.Y., C.B.O'C. and I.T. performed the experiments. J.G.A., B.F.M., A.K. and I.T. conducted correlative LM/EM. A.M. and R.P. developed the computational models. R.P. designed computer code and performed simulations. The manuscript was written by A.K., B.F.M. and A.M.

COMPETING FINANCIAL INTERESTS

The authors declare no competing financial interests.

Published online at http://dx.doi.org/10.1038/ncb3223
Reprints and permissions information is available online at www.nature.com/reprints

1. McIntosh, J. R., Molodtsov, M. I. & Ataullakhanov, F. I. Biophysics of mitosis. *Q. Rev. Biophys.* **45,** 147–207 (2012).
2. Walczak, C. E., Cai, S. & Khodjakov, A. Mechanisms of chromosome behaviour during mitosis. *Nat. Rev. Mol. Cell Biol.* **11,** 91–102 (2010).
3. Hayden, J. H., Bowser, S. S. & Rieder, C. L. Kinetochores capture astral microtubules during chromosome attachment to the mitotic spindle: direct visualization in live newt lung cells. *J. Cell Biol.* **111,** 1039–1045 (1990).
4. Tanaka, K. *et al.* Molecular mechanisms of kinetochore capture by spindle microtubules. *Nature* **434,** 987–994 (2005).
5. Kirschner, M. & Mitchison, T. Beyond self-assembly: from microtubules to morphogenesis. *Cell* **45,** 329–342 (1986).
6. Wan, X. *et al.* Protein architecture of the human kinetochore microtubule attachment site. *Cell* **137,** 672–684 (2009).
7. Brinkley, B. R. & Stubblefield, E. The fine structure of the kinetochore of a mammalian cell *in vitro*. *Chromosoma* **19,** 28–43 (1966).
8. McEwen, B. F., Ding, Y. & Heagle, A. B. Relevance of kinetochore size and microtubule-binding capacity for stable chromosome attachment during mitosis in PtK 1 cells. *Chromosome Res.* **6,** 123–132 (1998).
9. Hoffman, D. B., Pearson, C. G., Yen, T. J., Howell, B. J. & Salmon, E. D. Microtubule-dependent changes in assembly of microtubule motor proteins and mitotic spindle checkpoint proteins at PtK 1 kinetochores. *Mol. Biol. Cell* **12,** 1995–2009 (2001).
10. McEwen, B. F., Arena, J. T., Frank, J. & Rieder, C. L. Structure of the colcemid-treated PtK1 kinetochore outer plate as determined by high voltage electron microscopic tomography. *J. Cell Biol.* **120,** 301–312 (1993).
11. Cimini, D. *et al.* Merotelic kinetochore orientation is a major mechanism of aneuploidy in mitotic mammalian tissue cells. *J. Cell Biol.* **153,** 517–528 (2001).
12. Thrower, D. A., Jordan, M. A. & Wilson, L. Modulation of CENP-E organization at kinetochores by spindle microtubule attachment. *Cell Motil. Cytoskeleton* **35,** 121–133 (1996).
13. Feng, J., Huang, H. & Yen, T. J. CENP-F is a novel microtubule-binding protein that is essential for kinetochore attachments and affects the duration of the mitotic checkpoint delay. *Chromosoma* **115,** 320–329 (2006).
14. Cooke, C. A., Schaar, B., Yen, T. J. & Earnshaw, W. C. Localization of CENP-E in the fibrous corona and outer plate of mammalian kinetochores from prometaphase through anaphase. *Chromosoma* **106,** 446–455 (1997).
15. Kim, Y., Heuser, J. E., Waterman-Storer, C. M. & Cleveland, D. W. CENP-E combines a slow, processive motor and a flexible coiled coil to produce an essential motile kinetochore tether. *J. Cell Biol.* **181,** 411–419 (2008).
16. Magidson, V. *et al.* The spatial arrangement of chromosomes during prometaphase facilitates spindle assembly. *Cell* **146,** 555–567 (2011).
17. Loncarek, J. *et al.* The centromere geometry essential for keeping mitosis error free is controlled by spindle forces. *Nature* **450,** 745–749 (2007).
18. Wood, K. W. *et al.* Antitumor activity of an allosteric inhibitor of centromere-associated protein-E. *Proc. Natl Acad. Sci. USA* **107,** 5839–5844 (2010).
19. Kapoor, T. M. *et al.* Chromosomes can congress to the metaphase plate before biorientation. *Science* **311,** 388–391 (2006).
20. Cai, S., O'Connell, C. B., Khodjakov, A. & Walczak, C. E. Chromosome congression in the absence of kinetochore fibers. *Nat. Cell Biol.* **11,** 832–838 (2009).
21. Shrestha, R. L. & Draviam, V. M. Lateral to end-on conversion of chromosome-microtubule attachment requires kinesins CENP-E and MCAK. *Curr. Biol.* **23,** 1514–1526 (2013).
22. Collin, P., Nashchekina, O., Walker, R. & Pines, J. The spindle assembly checkpoint works like a rheostat rather than a toggle switch. *Nat. Cell Biol.* **15,** 1378–1385 (2013).
23. Roos, U. P. Light and electron microscopy of rat kangaroo cells in mitosis. II. Kinetochore structure and function. *Chromosoma* **41,** 195–220 (1973).
24. Goldstein, L. S. Kinetochore structure and its role in chromosome orientation during the first meiotic division in male *D. melanogaster*. *Cell* **25,** 591–602 (1981).
25. Church, K. & Lin, H. P. Kinetochore microtubules and chromosome movement during prometaphase in *Drosophila melanogaster* spermatocytes studied in life and with the electron microscope. *Chromosoma* **92,** 273–282 (1985).
26. Cimini, D., Moree, B., Canman, J. C. & Salmon, E. D. Merotelic kinetochore orientation occurs frequently during early mitosis in mammalian tissue cells and error correction is achieved by two different mechanisms. *J. Cell Sci.* **116,** 4213–4225 (2003).
27. Wollman, R. *et al.* Efficient chromosome capture requires a bias in the 'search-and-capture' process during mitotic-spindle assembly. *Curr. Biol.* **15,** 828–832 (2005).
28. Paul, R. *et al.* Computer simulations predict that chromosome movements and rotations accelerate mitotic spindle assembly without compromising accuracy. *Proc. Natl Acad. Sci. USA* **106,** 15708–15713 (2009).
29. Holy, T. E. & Leibler, S. Dynamic instability of microtubules as an efficient way to search in space. *Proc. Natl Acad. Sci. USA* **91,** 5682–5685 (1994).
30. Hill, T. L. Theoretical problems related to the attachment of microtubules to kinetochores. *Proc. Natl Acad. Sci. USA* **82,** 4404–4408 (1985).
31. Jones, J. T., Myers, J. W., Ferrell, J. E. & Meyer, T. Probing the precision of the mitotic clock with a live-cell fluorescent biosensor. *Nat. Biotechnol.* **22,** 306–312 (2004).
32. Rieder, C. L. & Alexander, S. P. Kinetochores are transported poleward along a single astral microtubule during chromosome attachment to the spindle in newt lung cells. *J. Cell Biol.* **110,** 81–95 (1990).
33. Kitajima, T. S., Ohsugi, M. & Ellenberg, J. Complete kinetochore tracking reveals error-prone homologous chromosome biorientation in mammalian oocytes. *Cell* **146,** 568–581 (2011).
34. DeLuca, J. G. *et al.* Hec1 and Nuf2 are core components of the kinetochore outer plate essential for organizing microtubule attachment sites. *Mol. Biol. Cell* **16,** 519–531 (2005).
35. Lancaster, O. M. *et al.* Mitotic rounding alters cell geometry to ensure efficient bipolar spindle formation. *Dev. Cell* **25,** 270–283 (2013).
36. O'Connell, C. B., Loncarek, J., Kalab, P. & Khodjakov, A. Relative contributions of chromatin and kinetochores to mitotic spindle assembly. *J. Cell Biol.* **187,** 43–51 (2009).
37. Kalinina, I. *et al.* Pivoting of microtubules around the spindle pole accelerates kinetochore capture. *Nat. Cell Biol.* **15,** 82–87 (2013).
38. Merdes, A. & De May, J. The mechanism of kinetochore-spindle attachment and polewards movement analyzed in PtK2 cells at the prophase-prometaphase transition. *Eur. J. Cell Biol.* **53,** 313–325 (1990).
39. Nicholson, J. M. & Cimini, D. How mitotic errors contribute to karyotypic diversity in cancer. *Adv. Cancer Res.* **112,** 43–75 (2011).
40. Silkworth, W. T. & Cimini, D. Transient defects of mitotic spindle geometry and chromosome segregation errors. *Cell Div.* **7,** 19 (2012).
41. Mazumdar, M., Sundareshan, S. & Misteli, T. Human chromokinesin KIF4A functions in chromosome condensation and segregation. *J. Cell Biol.* **166,** 613–620 (2004).
42. Wandke, C. *et al.* Human chromokinesins promote chromosome congression and spindle microtubule dynamics during mitosis. *J. Cell Biol.* **198,** 847–863 (2012).
43. Bakhoum, S. F., Genovese, G. & Compton, D. A. Deviant kinetochore-microtubule dynamics underlie chromosomal instability. *Curr. Biol.* **19,** 1937–1942 (2009).
44. Ganem, N. J., Godinho, S. A. & Pellman, D. A mechanism linking extra centrosomes to chromosomal instability. *Nature* **460,** 278–282 (2009).
45. Silkworth, W. T., Nardi, I. K., Scholl, L. M. & Cimini, D. Multipolar spindle pole coalescence is a major source of kinetochore mis-attachment and chromosome mis-segregation in cancer cells. *PLoS ONE* **4,** e6564 (2009).
46. Kleylein-Sohn, J. *et al.* Acentrosomal spindle organization renders cancer cells dependent on the kinesin HSET. *J. Cell Sci.* **125,** 5391–402 (2012).

METHODS

Cell culture, chemical treatments and live-cell microscopy. The human non-transformed hTERT-RPE1 cell line was purchased from Clontech in 2001 at passage number 118.5. Stocks of these cells at passage numbers 120–122 were generated in the Khodjakov laboratory and kept in liquid nitrogen. A stable clone (RPE1-18) that co-expresses CenpA–eGFP and centrin1–eGFP (both introduced by lentivirus)[16] was used in most of the experiments described here. Experiments that required visualization of fluorescent Mad2 were conducted in the RPE1$^{Mad2/Mad2-Venus}$ cell line provided by J. Pines, University of Cambridge[22]. All cell lines were grown in antibiotic-free DMEM supplemented with 10% FCS (Invitrogen) at 37 °C, 5% CO_2. For live-cell imaging, cells were grown on glass coverslips (no. 1 1/2) and mounted in Rose chambers containing CO_2-independent media (Invitrogen) supplemented with 10% FCS. In-house tests for mycoplasma (high-concentration Hoechst staining) are negative.

Microtubule depolymerization was induced by nocodazole (Sigma) at 3 μM. Motor activity of CenpE was inhibited with GSK-923295 (ref. 18) purchased from Haoyuan Chemexpress.

Multi-mode 3D time-lapse recordings were obtained on a Nikon TE-2000E PFS microscope with a 100X Plan Apo, NA 1.4 oil immersion objective lens. Fluorescence images were captured in a spinning-disc confocal mode (GSU-10, Yokogawa) on a back-illuminated Cascade 512B EM CCD (charge-coupled device) camera (Photometrics). DIC images were recorded on a Photometrics CoolSnap CF camera mounted on a different port of the same microscope. Full 3D volumes were recorded at each time point at 250-nm Z-steps (48–62 planes depending on cell thickness).

To visualize formation of the clear zone we first tracked 3D positions of mother centrioles and then rotated the 3D volume at each time point to fix the position of one mother centriole and the orientation of the spindle axis[47]. This processing allowed us to observe chromosome movement in the precisely transverse and axial views. Mother centrioles were tracked using FIJI with the standard tracking plugin. 3D coordinates of the centrioles and the images were then imported into MatLab. The image volume was padded with black (0 value) voxels to prevent cropping during rotation. The rotation was done in MatLab through two sequential steps, first in X–Y and then in Z. Rotated and aligned images were transferred back to FIJI. Maximal-intensity projections of the entire rotated volume were generated along the spindle axis (transverse view) and orthogonally to the spindle axis (axial view). Each view presented in Fig. 8 contains both centriole pairs and all kinetochores.

Incorporation of individual chromosomes into the spindle was observed under conditions that prevented cell rounding during mitosis. A coverslip with 3-μm microfabricated feet was placed on top of the coverslip with the growing cells. The contact between coverslips was maintained with negative pressure using a vacuum pump[48].

Fixed-cell immunofluorescence. Cells were pre-extracted in warm PEM buffer (100-mM PIPES, pH 6.9, 2.5-mM EGTA, 5-mM $MgCl_2$) supplemented with 0.5% Triton X-100 for 1 min and fixed with 1–2% glutaraldehyde for 10 min in PEM. Microtubules were visualized with a monoclonal anti-α-tubulin antibody (DM1a, Sigma; 1:200 dilution). Kinetochores were delineated with the following antibodies: rabbit αCenpF (Novus Biologicals, NB500-101; 1:400 dilution), mouse αCenpE antibody (Abcam, ab5093; 1:200 dilution), mouse αHec1 (Abcam, ab3613; 1:200 dilution), and rabbit αMis12 (provided by I. Cheeseman, Massachusetts Institute of Technology, USA; 1:400 dilution)[49]. Hoechst 33343 (1 μg ml^{-1}) was used to stain DNA (chromosomes). Inner kinetochores were visualized by means of CenpA–GFP fluorescence.

Wide-field images were recorded on a DeltaVision imaging system (Applied Precision) with a 100X NA 1.35 lens (Olympus). The images were captured with a CH-350 CCD camera (Photometrics) at a 69-nm $X-Y$ pixel size and 200-nm Z-steps. All images were deconvolved with the SoftWoRx 5.0 deconvolution software (Applied Precision) and objective lens-specific point spread functions.

Amira software (FEI) was used for surface rendering. The segmentation threshold for fluorescence images (Supplementary Fig. 2) was set at 25% of maximal intensity for each data set.

Quantification of fluorescence intensity and kinetochore volume. All measurements were conducted in ImageJ/FIJI and calculations were conducted in MS Excel. Integrated fluorescence intensity was measured within a 3D volume centred on a single kinetochore (whenever possible) or a small group of kinetochores (if their individual signals were not fully resolvable). The dimensions of the volume were set individually to include the entire object of interest (300–2,500 voxels, $10\times10\times3$–$25\times25\times4$ volumes). Background intensity for each measurement was measured in the same-dimensions volume positioned as close as possible to the object of interest. Kinetochore intensity was calculated by subtracting background intensity and dividing the result by the number of kinetochores in the volume. Intensities of multiple kinetochores (usually ~20) were measured in each cell. Mean fluorescence intensity per kinetochore was calculated for individual cells and then the mean value of per-cell averages was calculated. Alternatively, all kinetochores measured under a particular experimental condition were pooled together and the mean value was calculated for this pooled population. Results of both calculations are presented in the figures (Ks: total number of kinetochores; Cs: total number of cells). All values are normalized so that the mean intensity at NEB equals 1.

Kinetochore volumes were measured with the '3D Object Counter' routine included in the standard distribution of FIJI. As the amount of CenpF and Mis12 remains constant during late prophase–prometaphase, relative volumes occupied by kinetochores can be segmented at a constant threshold. Threshold values for segmentation were set at 20% of maximal signal intensity for CenpF and 25% for Hec1 data sets. These thresholds were empirically determined to yield maximal numbers of kinetochores per cell with minimal contamination by false objects after segmentation. As in intensity calculations, both mean values were calculated for per-cell averages and for the pooled populations (both values are presented in the Figures). All values are normalized so that the mean volume at NEB equals 1.

Mean values were compared using a two-tailed Student's t-test.

Correlative electron microscopy. Cells were fixed in 2.5% glutaraldehyde (Sigma) in PBS (pH 7.4–7.6). Differential interference contrast and fluorescence images were acquired at 0.2-μm Z-steps through the entire cell volume shortly after fixation. Post-fixation, embedding and sectioning were done as previously described[50]. Serial 80-nm thin sections were imaged at 80 kV on either a Zeiss 910 (Carl Zeiss) or JEOL 1400. Correlation of conspicuous morphological features between differential interference contrast and EM images was used to match the orientation and Z positions for individual focal planes and determine exact kinetochore positions.

Computational modelling. We consider that spindle assembly takes place in the spherical volume that was occupied by the nucleus before NEB. Implicitly, we assume, following ref. 27, that the RanGTP gradient focuses the microtubules into the nuclear sphere. This accelerates the search a few fold but has no effect on the error rate. Two centrosomes are placed at the opposite poles of the sphere at $-R_{cell}$ and $+R_{cell}$ positions. Each centrosome nucleates N_{MT} microtubules that search the space isotropically. Each microtubule is represented by a rod with zero thickness that undergoes dynamic instability. The plus end of a microtubule grows steadily until a catastrophe occurs leading to microtubule shortening. The frequency of catastrophe, as well as the growth and shrinkage rates, is constant (results have been found not to be sensitive to small variations of catastrophe frequencies). We use the optimal zero rescue frequency[28]. Microtubule dynamics are simulated by the Monte Carlo algorithm: a random number is generated between 0 and 1 with equal probability. At each computational step (with time increment $\Delta t = 1$ s) the microtubule switches to shortening if this random number is less than $[1-\exp(-f_{cat}\Delta t)]$. New microtubules grow in random directions and do not turn. In all cases, if a microtubule plus end extends beyond the nuclear sphere's boundary or encounters a chromosome arm, this microtubule undergoes catastrophe and shrinks all the way back to the centrosome.

The values for the number of microtubules generated by each centrosome (N_{MT}) and the four parameters of dynamic instability (v_g, v_s, f_{cat}, f_{res}) used in the simulations are presented in Supplementary Table 1. The radius of the nuclear/spindle sphere is set to match the geometry of mitosis in RPE1 cells[16]. Effects of the microtubule dynamic instability parameters have been previously explored and discussed[28]. In the current simulations, conservative values from the range explored in ref. 28 are used for v_g and v_s. The number of microtubules in the current simulations (600) is approximately twofold higher than in previous models (250; ref. 28). This change is introduced to account for the difference in spindle assembly time between HT-29 (15 min; ref. 28) and RPE1 (8 min; ref. 16) cells. The model indeed predicts slower absolute assembly time if the number of microtubules is lowered. However, the differences between the predictions in the three considered scenarios (see below) are not affected by the number of microtubules: relative differences in the assembly time as well as the predicted number of errors remain the same.

A second set of stable microtubules runs along the spindle axis and overlaps in the central part of the spindle. On the basis of microscopy data, this dense microtubule array forms shortly after NEB (1–2 min) and persists through prometaphase[16]. The centromeres become positioned on the surface of the nascent spindle shortly (~2 min) after NEB (Fig. 7 and ref. 45) and laterally interact with microtubule walls. In contrast to end-on attachments, lateral interactions can occur along the entire length of the microtubule and there is no evidence that these interactions require microtubules to undergo plus-end dynamic instability. Therefore, the nascent spindle in our simulations comprises stable microtubules whose plus ends do not contribute to capture. Geometry of the nascent spindle is derived from previously published data[16].

A microtubule plus end is instantly captured and stabilized on encountering a kinetochore. On capture, a new dynamic microtubule is nucleated at the same pole to replace the stabilized one.

Chromosomes are modelled as solid 3D cylinders with R_{CH} radius and I_{ch} length (Supplementary Table 1). The initial distribution of chromosomes

DOI: 10.1038/ncb3223

in the nuclear sphere and their orientation are random. Before capture, sister kinetochores are modelled as crescent-shaped objects (see Supplementary Table 1 and Supplementary Fig. 3 for dimensions) wrapped around the central part (equator) of the chromosome. The width w_{KT} and length h_{KT} of kinetochores are kept constant. On capturing a microtubule, the kinetochore crescent condenses into a small cylindrical object in τ_{comp} time. This kinetochore geometry reflects our experimental observations (Figs 1–4).

To complete computations with a reasonable time and avoid difficulty in tracking steric inter-chromosomal interactions, single chromosomes positioned at a fixed distance away from the pole–pole axis are considered in individual simulations. The simulations are then repeated for multiple chromosome positions and random orientations. To obtain the average value of the capture time (τ_{capt}), we multiplied the capture time of a single chromosome by the logarithm of the total number of chromosomes N_{CH} (Supplementary Table 1).

Four different scenarios are considered. In the first scenario, completely random distribution and orientation of chromosomes remains unaltered on microtubule capture. Kinetochores are shaped as crescents at the onset of spindle assembly and compact from crescents to discs in τ_{comp} after capture. In the second scenario, microtubule capture leads to rotation of the chromosome and alignment of the centromere axis (line connecting centres of sister kinetochores) along the captured microtubule in time τ_{rot}. Kinetochores are shaped as crescents at the onset of spindle assembly and compact from crescents to discs in τ_{comp} after capture. As the chromosome arms are largely normal to the pole–pole axis, the rotation primarily occurs around their longitudinal axis. In the third scenario, rapid lateral interactions with the stable microtubules of the nascent spindle result in a rapid decrease of the angle between the centromere axis and spindle axis (line connecting the centrosomes) in time τ_{rot}. The angle of chromosome rotation is limited by the ability of kinetochores to maintain direct contact with stable microtubules, which in turn depends on the size of the kinetochore crescent. Kinetochores are shaped as crescents at the onset of spindle assembly and compact from crescents to discs in τ_{comp} after capture. Compaction initiates only after end-on microtubule capture and completes in τ_{comp}. Finally, in the fourth scenario the crescents are small at the onset of the search, with the initial gap size of 0.76 μm. In the next 30 s, the crescents grow linearly so that the gap decreases to its final size (0.01 to 0.76 μm in various simulations). The time of crescent growth is constant, irrespective of the final gap size. Lateral interactions decrease the angle between the centromere axis and the spindle axis as in scenario iii; respective rate of rotation is very fast, a few seconds, in this case. Then, the end-on microtubule capture leads to additional rotation of the chromosome and alignment of the centromere axis (line connecting centres of sister kinetochores) along the captured microtubule in time τ_{rot}. Kinetochores compact from crescents to discs in τ_{comp} after end-on microtubule capture.

In the most simplistic simulations (scenario i), microtubule capture is not expected to change the position or orientation of the chromosome[27,29,30]. Rotation of the centromere considered in the second, third and fourth scenarios inevitably shifts the chromosome from its original position. However, in 80% of the cases the mean value of the displacement caused by the brief rapid movement during the initial interaction between kinetochores and microtubules is <1 μm in RPE1 cells[16]. Such a small translation does not significantly affect the probability of subsequent microtubule capture. Larger translations are rare and therefore not considered in the current model.

All simulations are carried out for various gap sizes between the crescent sister kinetochores (Supplementary Table 1). Computational data presented in the manuscript are obtained from running simulations for each set of the parameters at least 1,000 times.

The numerical codes are implemented with C programming language. Numerical experiments are performed on an IBM quad core Intel CPU server. The code of the simulation is available as Supplementary Data.

47. Sikirzhytski, V. *et al.* Direct kinetochore-spindle pole connections are not required for chromosome segregation. *J. Cell Biol.* **206,** 231–243 (2014).
48. Le Berre, M., Aubertin, J. & Piel, M. Fine control of nuclear confinement identifies a threshold deformation leading to lamina rupture and induction of specific genes. *Integr. Biol.* **4,** 1406–1414 (2012).
49. Kline, S. L., Cheeseman, I. M., Hori, T., Fukagawa, T. & Desai, A. The human Mis12 complex is required for kinetochore assembly and proper chromosome segregation. *J. Cell Biol.* **173,** 9–17 (2006).
50. Rieder, C. L. & Cassels, G. Correlative light and electron microscopy of mitotic cells in monolayer cultures. *Methods Cell Biol.* **61,** 297–315 (1999).

DOI: 10.1038/ncb3223

nature cell biology

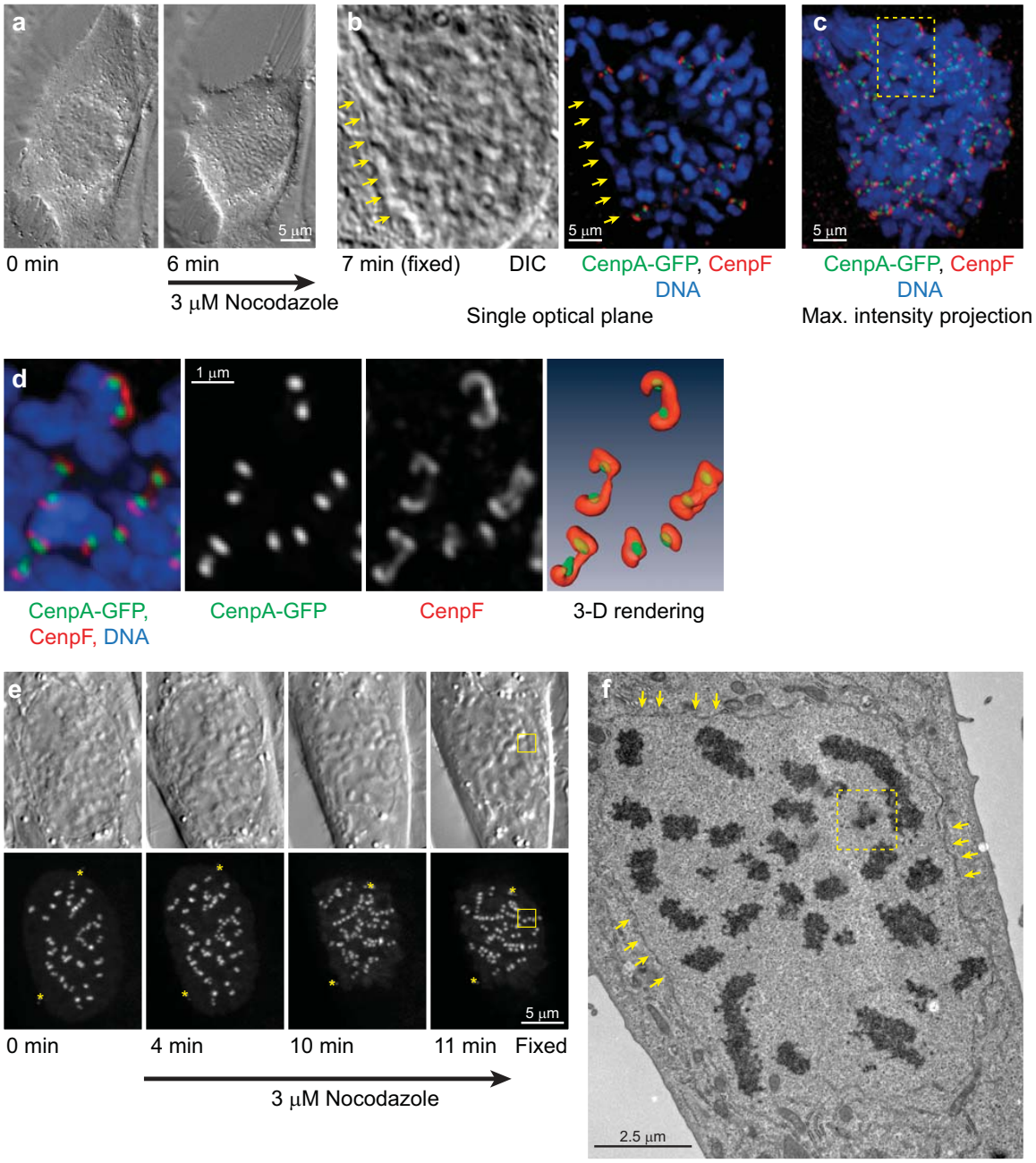

Supplementary Figure 1 Experimental approach used to characterize the 'virgin' kinetochore architecture at spindle assembly onset. **(a)** Selected differential interference contrast (DIC) images (individual planes) illustrating a prophase cell immediately prior to the addition of 3-μM nocodazole (0 min) and at nuclear envelope breakdown (NEB, 6 min). The cell was fixed with 1% glutaraldehyde immediately after NEB. **(b)** A single optical plane near the middle of the cell shown after fixation in DIC and fluorescence. Notice that chromosomes (blue, Hoechst 33343) appear to be still aligned along the remnants of the nuclear envelope (arrows) indicating that the cell was fixed at the onset of mitosis. **(c)** Maximal intensity projection of the entire cell. **(d)** Higher magnification view of kinetochores from the boxed area in (c). The outer layer (red, CenpF) is enlarged and largely encircles the centromere. Inner kinetochores (green, CenpA-GFP) remain compact. Maximal intensity projections of a local sub-volume and surface-rendered reconstruction segmented at 25% of maximal intensity. **(e, f)** Treatment history of the cell shown in Figure 3e,f. **(e)** Selected DIC and corresponding fluorescent images (CenpA-GFP and Centrin-GFP) depicting a different cell prior to the addition of 3-μM nocodazole (0 min), during late prophase (4 min), at (NEB, 10 min), and immediately after fixation (11 min). Asterisks indicate the location of the centrioles. The boxed area in panels D and E is shown in Figure 2B at higher magnification. **(f)** Electron-microscopy image of the same cell. Remnants of the nuclear envelope are clearly visible (yellow arrows). The box denotes the centromere presented in Figure 2b.

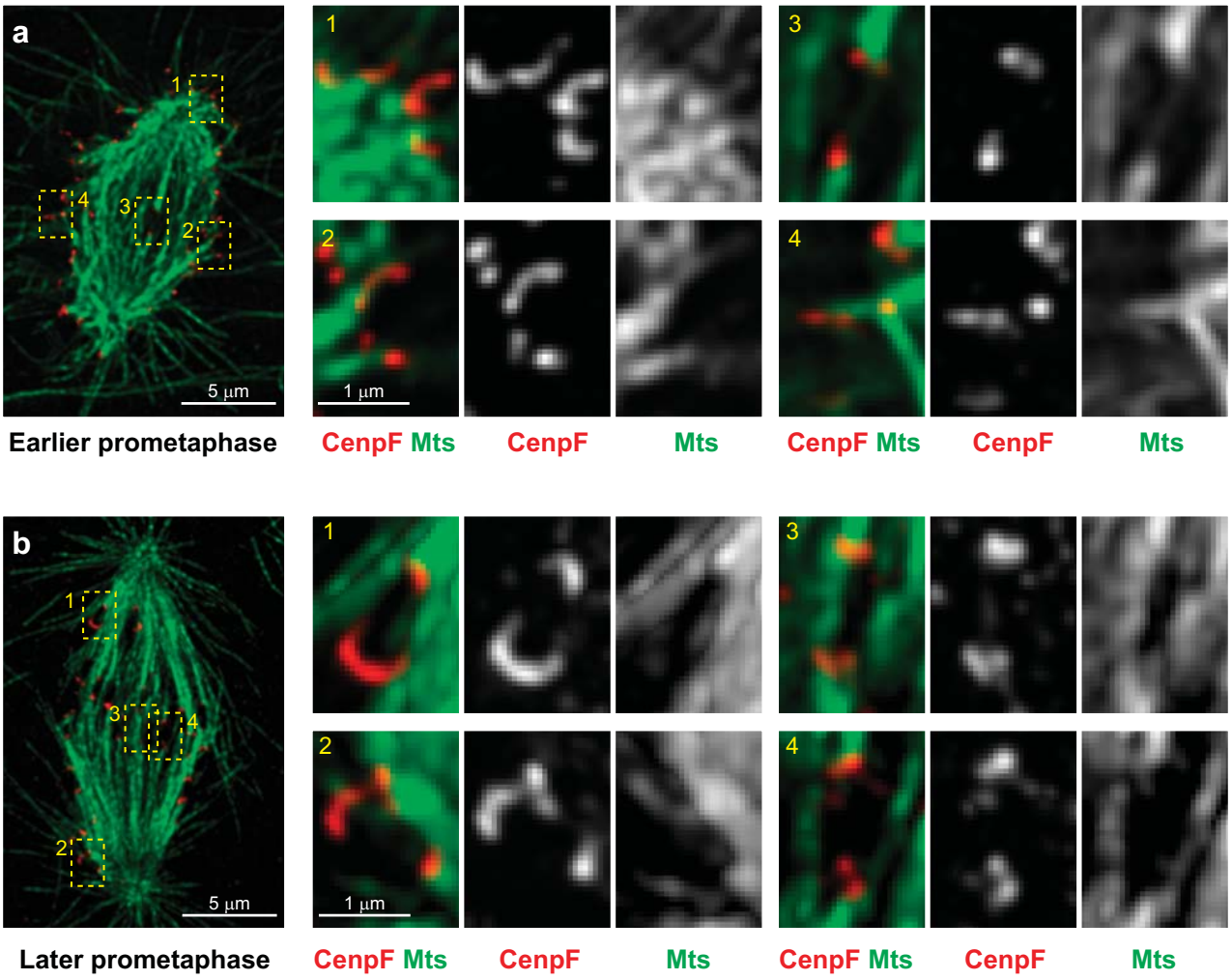

Supplementary Figure 2 Kinetochore outer layer compaction correlates with the formation of end-on microtubule attachment. **(a)** In earlier prometaphase cells, kinetochores with an enlarged outer layer are present throughout the cell (insets 1, 2). However, a few kinetochores that display prominent end-on attachment to microtubule bundles are compact (insets 3, 4). **(b)** In later prometaphase, at least one kinetochore displays an enlarged outer layer on each monooriented chromosome and these enlarged kinetochores lack end-on microtubule attachments (insets 1, 2). In contrast, both sister kinetochores on bioriented chromosomes are compact (insets 3, 4). Whole-cell images are maximal-intensity projections that include all kinetochores in the cell. Individual kinetochores are shown as maximal-intensity projections of local sub-volumes.

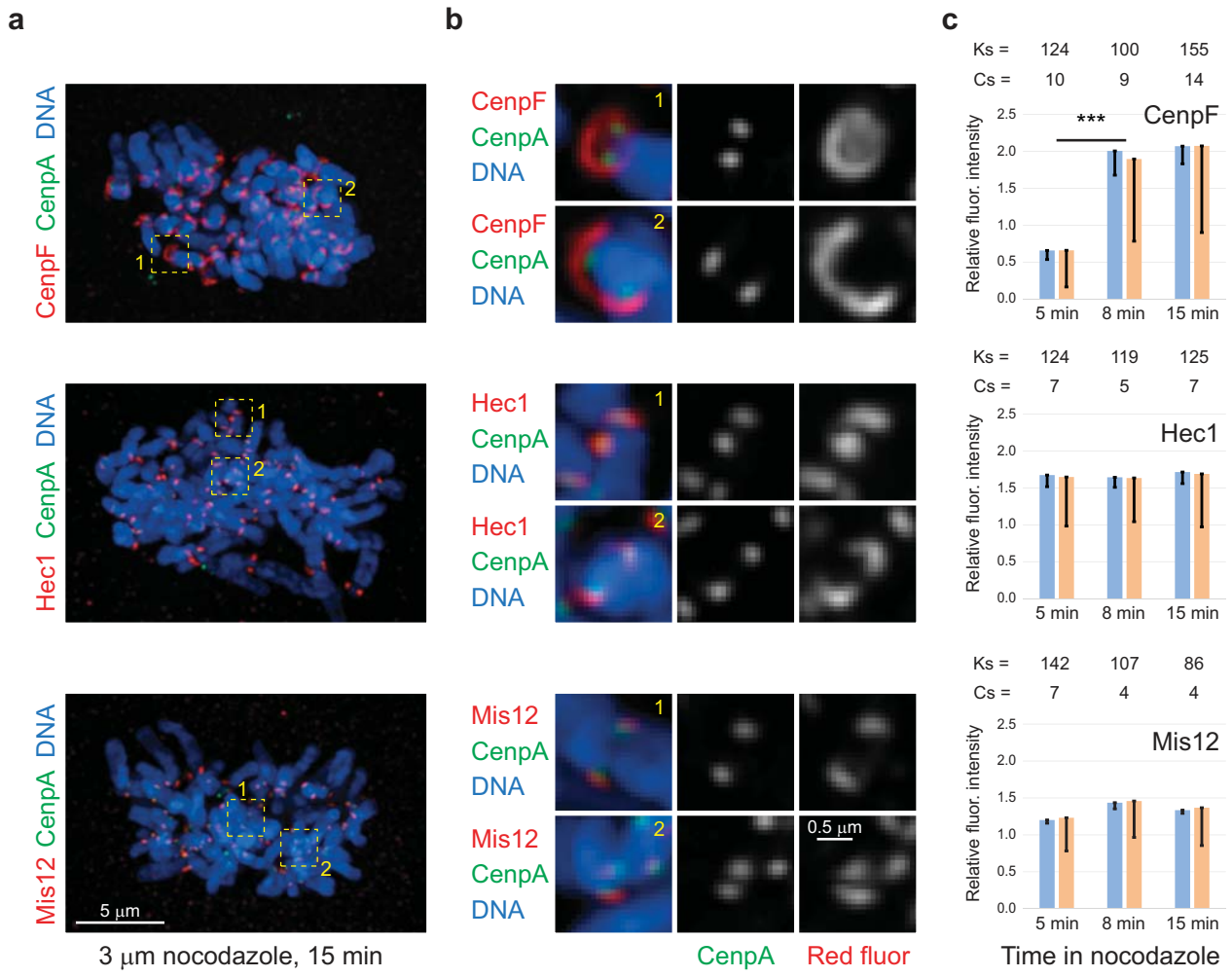

Supplementary Figure 3 Distribution and amounts of various kinetochore proteins in the absence of microtubules. **(a)** Maximal intensity projections (include all kinetochores) depicting RPE1 cells after 15-min exposure to 3-μM nocodazole. Notice that the analyses were only on cells that had formed a metaphase plate prior to the addition of nocodazole as evident from the pattern of chromosome distribution and positions of centrosomes on the opposite sides of the plates. **(b)** Examples of individual kinetochores from the boxed areas in (a), shown at higher magnification. CenpF forms large crescents that can completely encircle the centromere. The distributions of Hec1 and Mis12 also appear to broaden albeit to lesser extents than CenpF. **(c)** Relative fluorescence intensities of kinetochores at various times after addition of nocodazole. The amount of the outer layer protein CenpF (red) remains at the level typical for untreated metaphase (compare with . Fig.1c, $p > 0.3$, two-tailed Student's t-test for both blue vs. blue and yellow vs. yellow bars.) and then increases approximately threefold. The amount of Hec1 instantly increases approximately twofold over the levels typical for kinetochores during metaphase (compare with Fig.1c, $p < 0.0001$, two-tailed Student's test for both blue vs. blue and yellow vs. yellow bars.). The amount of Mis12 in nocodazole-treated cells is not significantly different from the metaphase level (compare with Fig.1c, $p > 0.09$, two-tailed Student's test for both blue vs. blue and yellow vs. yellow bars). Blue bars in (c) are mean kinetochore intensity calculated as mean of mean values for multiple kinetochores in individualcells (n values above the bars, Cs; cells) Error bars represent s.e.m. Yellow bars are mean values calculated for all kinetochores pooled from all cells in that class (n values above the bars, Ks; kinetochores). Error bars represent s.d.

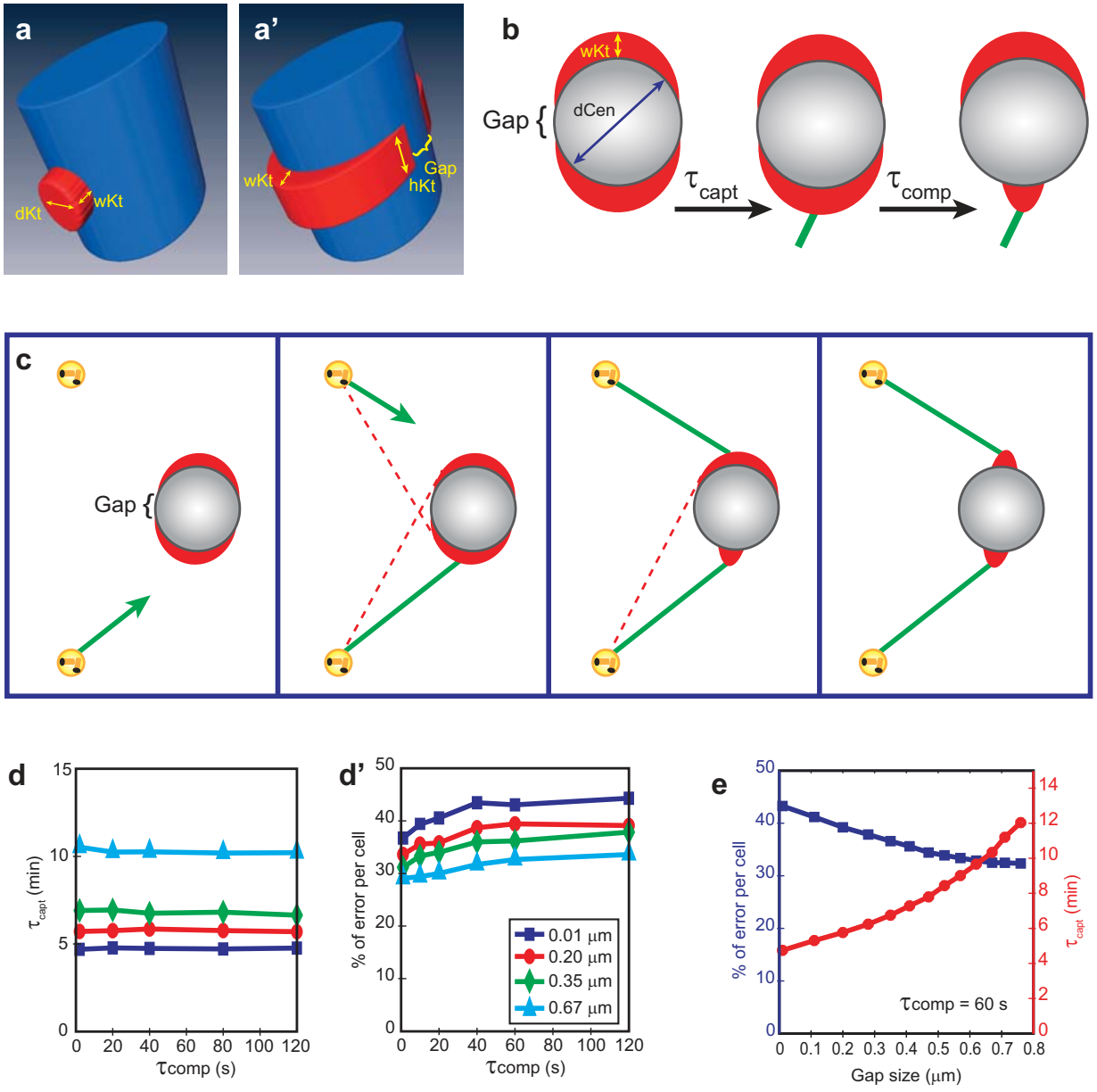

Supplementary Figure 4 Effects of kinetochore enlargement-compaction on the efficiency and fidelity of capture-driven spindle assembly. **(a-a')** Architecture of the virgin (unattached) centromere considered in the previous computational models of spindle assembly (a) vs. the current model (a'). dKt, diameter of the discoid kinetochore in previous models; wKt and hKt, width and height of the expanded crescent-like kinetochore; Gap, segment of the centromere not covered by the kinetochore outer layer. **(b)** Diagram showing the changes in the centromere architecture considered in the minimalistic computational model. τ_{capt}, time from the onset of spindle assembly to end-on attachment; τ_{comp}, duration of the conversion from the expanded crescent to compact architecture of the kinetochore. **(c)** Sequence of events envisioned in the minimalistic model. Attachment triggers kinetochore compaction but does not affect orientation of the centromere. Green lines represent properly attached microtubules, red lines - potential erroneous attachments. **(d, d')** Duration of spindle assembly and frequency of errors predicted for various final gap sizes, and various durations of kinetochore compaction. Notice that both efficiency and accuracy of spindle assembly remain nearly constant at $\tau_{comp} > 60$ s. **(e)** Frequency of errors and duration of spindle assembly predicted for centromeres with various final gap sizes for specific values of τ_{expand} and τ_{comp}.

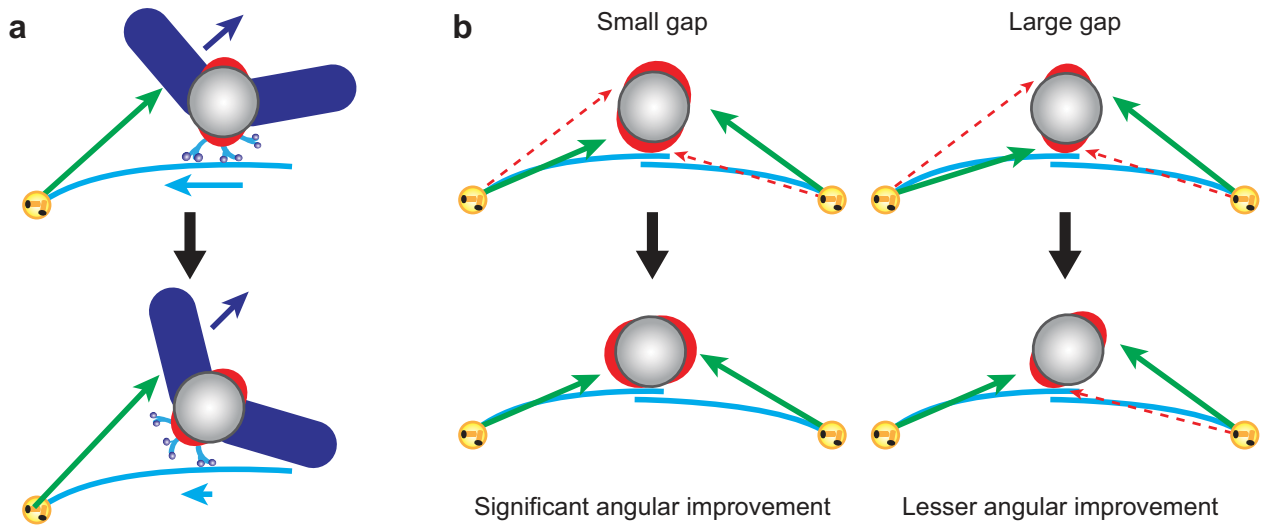

Supplementary Figure 5 Rotation of the centromere due to lateral interactions between kinetochores and microtubules. **(a)** Opposition of inward-directed forces generated at the kinetochore (dynein) and outward forces acting on chromosome arms (chromokinesins) rotate the centromere positioned on the surface of the spindle. **(b)** Centromeres with a small gap between sister kinetochores can rotate significantly while maintaining constant contact with microtubules. In contrast, rotation of centromeres with a large gap between sister kinetochores is sterically limited due to small kinetochores losing direct contact with microtubules. As the result, after rotation large sister kinetochores are primarily exposed to their proximal poles (green arrows) and shielded from the distal poles by the centromere. Due to the lesser angular improvement, smaller sister kinetochores remain exposed to both proximal and distal poles (red arrows).

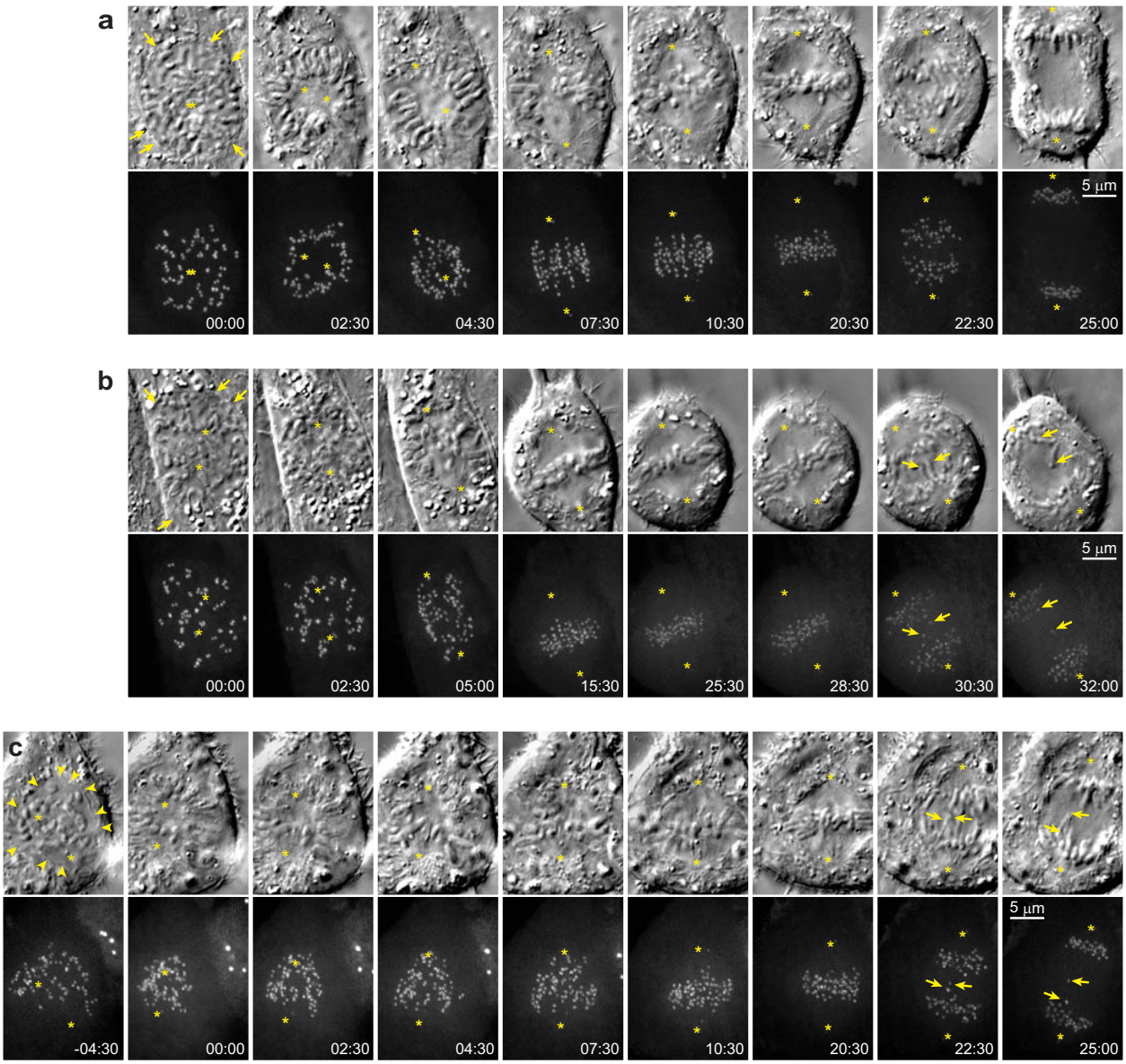

Supplementary Figure 6 Conventional (not rotationally aligned) views of the cells presented in Figure 8. **(a)** Normal spindle assembly in an RPE1 cell (see Figure 7a). **(b)** An untreated RPE1 cell with lagging chromosomes (Figure 7B). **(c)** An RPE1 cell that assembled its spindle after nocodazole washout. Notice that drug washout is initiated soon after NEB when remnants of the nuclear envelope are still present in the cell (arrowheads). Each time point is shown in DIC (medial slices from 3-D volumes) and GFP-fluorescence (maximal intensity projections). Asterisks denote mother centrioles (labeled with centrin-GFP). Arrows point at NEB remnants in DIC images and lagging chromosomes in fluorescent images. Time in minutes : seconds from NEB (a, b) or from completion of nocodazole washout (c).

Table S1. Parameters used in the computational models

N_{CH}	Number of chromosomes in the simulations	1x46
N_{KT}	Number of kinetochores in the simulations	2x46
N_{MT}	Number of dynamic microtubules from each pole	600
R_{nuc}	Radius of the nuclear/spindle sphere	5 µm
R_{cen}	Radius of the chromosome (centromere)	0.35 µm
l_{chr}	Chromosome length	4 µm
w_{KT}	Width of the kinetochore crescent	0.2 µm
h_{KT}	Height of the kinetochore crescent	0.2 µm
l_{KT}	Length of the compacted kinetochore	0.1 µm
r_{KT}	Radius of the compacted kinetochore	0.05 µm
v_g	Microtubule growth rate	0.5 µm/s
v_s	Microtubule shortening rate	1 µm/s
f_{cat}	Microtubule catastrophe frequency	0, 0.01 s^{-1}
f_{res}	Rescue frequency of MT	0
τ_{comp}	Condensation of crescent KT	~ 60 s
τ_{rot}	Rotation time of chromosome	~ 30 s
τ_{expand}	Duration of the kinetochore outer layer expansion	~ 30 s
Gap	Final size of the centromere segments that separate expanded outer layers of sister kinetochores	0.01-0.76 µm

Supplementary Table Legends

Supplementary Table 1 Parameters used in the computational models. The table presents numeric values for the parameters of microtubule dynamic instability as well as numbers of chromosomes/kinetochores, and sizes of mitotic components that were used in the computational simulations.
Supplementary Computer Code legend
The simulation was written in *C* programming language and tested on an intel quad-core CPU.

Supplementary Video Legends

Supplementary Video 1. Incorporation of individual chromosomes into the spindle. Related to Figure 6. Mad2 fluorescence (green) is overlaid on phase contrast (grey). The video starts with 3 centromeres on the lower left side of the spindle showing Mad2 fluorescence. The chromosome nearest the spindle equator has already initiated congression at the start of filming and rapidly moves to the equator where it loses Mad2 fluorescence. The other two centromeres show one or more rapid rotations (lasting no more than two consecutive frames at 30-s intervals) before initiating congression and loss of Mad2 fluorescence. Time in minutes : seconds from the start of the video.

Supplementary Video 2. Axial and transverse views of spindle assembly in control and nocodazole treated cells. Related to Figure 8. A typical control cell is shown in the left panels, a control cell with lagging chromosomes in the middle panels, and a cell subjected to nocodazole treatment followed by washout of the drug in the right panels. Note that the typical control cell forms the clear middle zone with all centromeres confined to the periphery (frames 3-13). The fluorescent dots in the middle of the transverse views are the centrioles. Time in minutes : seconds from NEB (left and central panels) or from completion of nocodazole washout (right panel).

Supplementary Video 3. A typical control cell as conventionally seen in the light microscope (not rotationally aligned). The video shows the medial plane of DIC and the maximal-intensity projection of GFP-fluorescence for the cell shown in Figure 8a and the left panels of Supplementary Video 2. Note that clear zone formation in the central spindle is not evident in this view. Time in minutes : seconds from NEB.

Supplementary Video 4. A control cell with lagging and lost chromosomes as conventionally seen in the light microscope (not rotationally aligned). The video shows the medial plane of DIC and the maximal-intensity projection of GFP-fluorescence for the cell shown in Figure 8b and the middle panels of Supplementary Video 2. Note that the difference in clear zone formation between a typical control cell (Supplementary Video 3) and one leading to lost chromosomes (this video) is not detected. Hence, detection of the lack of clear zone formation requires that data sets be rotationally aligned. Time in minutes : seconds from NEB.

Supplementary Video 5. A cell treated with nocodazole in prophase followed by drug washout after NEB as conventionally seen in the light microscope (not rotationally aligned). The video shows the medial plane of DIC and the maximal-intensity projection of GFP-fluorescence for the cell shown in Figure 8c and the right panels of Supplementary Video 2. As in Supplementary Video 4, the lack of a clear zone is not detected unless data sets are rotationally aligned. Time in minutes : seconds from completion of nocodazole washout.